Astronomy & Astrophysics manuscript no. distro˙paper
May 30, 2013

© ESO 2013

arXiv:1304.7770v3 [astro-ph.GA] 29 May 2013

A *Herschel* [C II] Galactic plane survey I: the global distribution of ISM gas components*

J. L. Pineda, W. D. Langer, T. Velusamy, and P. F. Goldsmith

Jet Propulsion Laboratory, California Institute of Technology, 4800 Oak Grove Drive, Pasadena, CA 91109-8099, USA
e-mail: `Jorge.Pineda@jpl.nasa.gov`

Received January 30, 2013; accepted April 11, 2013

ABSTRACT

Context. The [C II] 158μm line is an important tool for understanding the life cycle of interstellar matter. Ionized carbon is present in a variety of phases of the interstellar medium (ISM), including the diffuse ionized medium, warm and cold atomic clouds, clouds in transition from atomic to molecular, and dense and warm photon dominated regions (PDRs).

Aims. Velocity–resolved observations of [C II] are the most powerful technique available to disentangle the emission produced by these components. These observations can also be used to trace CO–dark H_2 gas and determine the total mass of the ISM.

Methods. The Galactic Observations of Terahertz C+ (GOT C+) project surveys the [C II] 158μm line over the entire Galactic disk with velocity–resolved observations using the *Herschel*/HIFI instrument. We present the first longitude–velocity maps of the [C II] emission for Galactic latitudes $b = 0^\circ$, $\pm 0.5^\circ$, and $\pm 1.0^\circ$. We combine these maps with those of H I, ^{12}CO, and ^{13}CO to separate the different phases of the ISM and study their properties and distribution in the Galactic plane.

Results. [C II] emission is mostly associated with spiral arms, mainly emerging from Galactocentric distances between 4 and 10 kpc. It traces the envelopes of evolved clouds as well as clouds that are in the transition between atomic and molecular. We estimate that most of the observed [C II] emission is produced by dense photon dominated regions (~47%), with smaller contributions from CO–dark H_2 gas (~28%), cold atomic gas (~21%), and ionized gas (~4%). Atomic gas inside the Solar radius is mostly in the form of cold neutral medium (CNM), while the warm neutral medium (WNM) gas dominates the outer galaxy. The average fraction of CNM relative to total atomic gas is ~43%. We find that the warm and diffuse CO–dark H_2 is distributed over a larger range of Galactocentric distances (4–11 kpc) than the cold and dense H_2 gas traced by ^{12}CO and ^{13}CO (4–8 kpc). The fraction of CO-dark H_2 to total H_2 increases with Galactocentric distance, ranging from ~20% at 4 kpc to ~80% at 10 kpc. On average, CO-dark H_2 accounts for ~30% of the molecular mass of the Milky Way. When the CO–dark H_2 component is included, the radial distribution of the CO–to–H_2 conversion factor is steeper than that when only molecular gas traced by CO is considered. Most of the observed [C II] emission emerging from dense photon dominated regions is associated with modest far–ultraviolet fields in the range $\chi_0 \simeq 1 - 30$.

Key words. ISM: atoms —ISM: molecules — ISM: structure — Galaxy: structure

1. Introduction

The transition from atomic to molecular clouds, the formation of stars within high density regions, the radiative feedback from newly formed stars, and the disruption of molecular clouds and termination of star formation are of great astrophysical interest as they are processes governing the evolution of galaxies in our Universe. In the Milky Way the evolution of the interstellar medium (ISM) has traditionally been studied with radio continuum and Hα observations for the ionized component (e.g. Haffner et al. 2009), with observations of the H I 21 cm line for the atomic gas component (e.g. Kalberla & Kerp 2009), and with rotational transitions of the CO molecule for the dense molecular gas component (e.g. Dame et al. 2001). But observations of the transition between these different stages of evolution with velocity–resolved observations required to separate different gas components along the line–of–sight (LOS) have been missing.

The [C II] 158μm fine–structure transition is an excellent tracer of the different stages of evolution of the ISM. As ionized carbon (C^+) can be found throughout the ISM and can be excited by collisions with electrons, H I, and H_2, the [C II] line traces the warm ionized medium, the warm and cold diffuse atomic medium, and warm and dense molecular gas. The [C II] 158μm line is the main coolant of the diffuse ISM and therefore plays a key role in the thermal instability that converts from warm and diffuse atomic clouds to cold and dense clouds. As the [C II] intensity is sensitive to column density, volume density, and kinetic temperature, it can be used to determine the physical conditions of the line–emitting gas.

The first sensitive all sky survey of line emission in the wavelength range between 100μm and 1 cm was carried out with the Far-Infrared Spectrometer (FIRAS) on COBE (Bennett et al. 1994). The angular resolution of COBE was 7° and the spectral resolution of FIRAS was about 1000 km s^{-1} for the [C II] 158μm and [N II] 205μm lines. The COBE map showed that [C II] is widespread over the Galactic plane and that it is the brightest far-infrared line. COBE also found a correlation between the [C II], [N II], and far–infrared (FIR) continuum emission, suggesting that [C II] might be a good tracer of star-formation activity in galaxies. The balloon-borne BICE mission (Nakagawa et al. 1998) observed [C II] in the inner Galactic plane with 15′ angular resolution and 175 km s^{-1} velocity resolution. This mission gave better constraints on the latitudinal distribution of the Galactic [C II] emission. The COBE and BICE missions did not have the required angular and velocity resolution to resolve spatially and in velocity individual clouds in the Galactic plane. The Kuiper Airborne Observatory allowed the study of a handful of H II regions with velocity-resolved [C II] observations (e.g Boreiko et al. 1988; Boreiko & Betz 1991). These observations, and also those recently obtained with *Herschel* (e.g. Ossenkopf et al. 2012) and SOFIA (e.g. Graf et al. 2012), were mostly limited to hot and dense photon–dominated regions (PDRs) associated with massive star-forming regions.

---

* *Herschel* is an ESA space observatory with science instruments provided by European-led Principal Investigator consortia and with important participation from NASA.

Far–infrared (FIR) dust continuum emission has been widely used as a mass tracer of the ISM, and several high–resolution, large–scale, sensitive maps of the Galactic plane exist (Carey et al. 2009; Molinari et al. 2010). Dust continuum emission is the result of the integrated contribution of different ISM components distributed along the line–of–sight. Therefore, it is impossible to use this emission to isolate and study the different contributing ISM components, particularly for observations of the Galactic plane.

The *Herschel* (Pilbratt et al. 2010) Open Time Key Project Galactic Observations of Terahertz C+ (GOT C+; Langer et al. 2011) provides the first high–angular resolution (12″), velocity–resolved (0.1 km s^{-1}) observations of the [C II] line in the Galactic disk, allowing us to resolve individual clouds and to separate the different ISM components along the line–of–sight. The GOT C+ survey consists of ∼500 LOSs distributed in a volume-weighted sampling of the Galactic disk. We have complemented our GOT C+ [C II] data with observations of the H I 21 cm line, tracing diffuse atomic gas, and of CO and its isotopologues, tracing the dense molecular gas.

In this paper we present the full GOT C+ Galactic plane survey. We use the kinematic information provided by high velocity resolution observations of [C II], obtained with the HIFI (de Graauw et al. 2010) instrument on *Herschel*, together with complementary CO and H I surveys to study the structure of the galaxy and to characterize the distribution of the different components of the interstellar medium in the Milky Way.

Neutral atomic hydrogen represents the dominant gas component of the interstellar medium in galaxies. This H I gas is predicted to exist in two phases in rough thermal pressure equilibrium (Pikel'Ner 1968; Field et al. 1969; Wolfire et al. 1995); the cold neutral medium ($n_{\rm H} \simeq 50\,{\rm cm}^{-3}$; $T_{\rm kin} \simeq 80$ K; CNM) and the warm neutral medium ($n_{\rm H} \simeq 0.5\,{\rm cm}^{-3}$; $T_{\rm kin} \simeq 8000$ K; WNM). Note, however, that gas in thermally unstable conditions has been observed (e.g Dickey et al. 1977; Heiles & Troland 2003) and predicted in numerical simulations (see Vázquez-Semadeni 2012, and references therein). The atomic gas component has been extensively mapped using the H I 21 cm line in the Milky Way and external galaxies. But this line in emission traces only the total column of gas along the line–of–sight (assuming that it is optically thin), and therefore it is impossible to disentangle the relative contribution from gas in the CNM or WNM. H I absorption studies of nearby clouds in the foreground of extragalactic continuum sources have provided constraints on the relative fraction of the CNM and WNM, suggesting that 60% of the gas is in the WNM and 40% is in the CNM (Heiles & Troland 2003). But these observations are limited to a small number of sources distributed mostly at high Galactic latitudes, thus corresponding only to the local ISM. We therefore lack the knowledge about the distribution and conditions of the CNM and WNM over the entire Galactic disk. The [C II] 158μm line is also a tracer of the diffuse neutral gas but has the advantage that it is also sensitive to the density and temperature of the gas. In particular, because of the density contrast between the CNM and WNM, for a given H I column density the [C II] emission associated with the WNM is expected to be a factor of ∼20 weaker than that associated with the CNM (Wolfire et al. 2010). We can therefore use the GOT C+ [C II] emission in combination with H I to study the distribution and properties of the WNM and CNM over the entire Galactic disk.

The mass of molecular clouds has traditionally been traced using observations of the CO molecule. However, the column density from the cloud exterior to the location where hydrogen becomes molecular is smaller than that required for carbon to become molecular in the form of CO. It is therefore expected that in the outer parts of molecular clouds a significant fraction of the H_2 is associated with C^+ and C^0 instead of with CO. This gas is called "hidden–H_2" or "dark–H_2" gas (see Grenier et al. 2005; Langer et al. 2010; Wolfire et al. 2010). In this paper we will refer to this component as "CO–dark H_2 gas". Indirect observations of gamma–rays (Grenier et al. 2005) and dust continuum emission (Planck Collaboration et al. 2011) suggest that 30–50% of the molecular mass in the Galaxy is not traced by CO. The preliminary results from GOT C+, based on a sample of 16 LOSs, reached a similar conclusion (Langer et al. 2010; Velusamy et al. 2010). Velusamy et al. (2013) used a Gaussian decomposition approach to study the GOT C+ LOS in the inner Galaxy, $-90° < l < 57°$, discussing the distribution of the [C II] velocity components as a function of Galactocentric distance and the distribution of CO–dark H_2 gas as function cloud type (diffuse clouds, transition clouds, and dense clouds traced by ^{13}CO). A more detailed analysis of the Gaussian decomposition of the GOT C+ [C II] emission in the inner galaxy will be presented in Langer et al. (2013) in preparation. Note that some of the H_2 gas might not be traced by CO due to the lack of sensitivity of the CO observations. In the Taurus molecular cloud, Pineda et al. (2010a) found that 23% of the total mass is in the outskirts of the cloud where neither ^{12}CO nor ^{13}CO could be detected in single pixels, but both isotopologues could be readily measured by averaging pixels over a large area.

A significant fraction of the FIR line and continuum emission in galaxies originates from dense photon–dominated regions (or photodissociation regions; or PDRs; see Hollenbach & Tielens 1999 and references therein). In PDRs the chemistry and thermal balance is dominated by the influence of far–ultraviolet photons from massive stars. Therefore, PDRs are the best sites for studying the radiative feedback from newly formed massive stars on their progenitor molecular gas, a process that plays a key role in the regulation of star–formation in galaxies. The [C II] line is a very bright tracer of PDRs and, together with fine–structure transitions of [O I] and [C I] and rotational transitions of CO, can be used to determine the physical conditions of the line–emitting regions. The FUV field intensity is a key parameter for PDRs and is closely related to the massive star–formation activity around PDRs. The FUV field is often measured in units of the Draine (1978) field[1] defined as the average FUV intensity in the local ISM. Kaufman et al. (1999) showed that the ratio of [C II] to CO is a good tracer of the strength of the FUV field in the galaxy. Using this line ratio in a sample of 16 LOSs, Pineda et al. (2010b) found that most of the dense PDRs have FUV fields lower than 100 times the interstellar FUV field. With the complete GOT C+ survey, we can use the [C ii]/CO ratio to trace the strength of the FUV radiation field over the entire Galactic disk.

---

[1] The average FUV intensity of the local ISM is $2.2{\times}10^{-4}$ erg $\rm cm^{-2}\,s^{-1}\,sr^{-1}$ (Draine 1978). The Draine field is isotropic (i.e. a given point is illuminated from 4π steradians), while the surface of the clouds considered here are only illuminated from 2π steradians, therefore the rate of photoreactions at the cloud surface are half of what they would be with the Draine field.

This paper is organized as follows. In Section 2 we describe the GOT C+ observations and data reduction. We also describe the observations of ancillary CO and H i data. In Section 3.1 we present position–velocity maps of the [C ii] emission and relate them to the spiral structure of the Milky Way. In Section 3.2, we present the distribution of the [C ii], H i, and CO emissivities as a function of Galactocentric distance. In Section 4, we combine the [C ii], H i, and CO emission to identify the different ISM components and determine their contribution to the observed [C ii] emission. We describe the distribution of the warm and cold neutral medium atomic gas components in Section 5.1. In Section 5.2, we study the radial distribution of the CO–dark H_2 gas component and compare it to that of molecular gas traced by CO and ^{13}CO. In Section 6 we present a determination of the FUV field distribution in the Galactic plane. We summarize our results in Section 7.

2. Observations

2.1. [C ii] observations

We surveyed the Galactic plane in the [C ii] $^2P_{3/2} \rightarrow {}^2P_{1/2}$ fine structure line at 1900.5469 GHz (rest frequency) with the HIFI (de Graauw et al. 2010) instrument on–board the *Herschel* space observatory (Pilbratt et al. 2010). These observations are part of the *Herschel* Open Time Key Project Galactic Observations of Terahertz C+ (GOT C+), which is devoted to studying the [C ii] 158 μm line over a wide range of environments in the Galactic plane, the Galactic center, and in the Outer Galaxy Warp. The GOT C+ Galactic plane survey consists of 452 LOSs distributed in an approximately volume–weighted sample of the Galactic plane. We present a selection of GOT C+ lines–of–sight in [C ii], H i, and ^{12}CO emission in Figure 1. The entire data set is presented as a set of position–velocity maps in Figure 2 and in Appendix B. We sampled in Galactic longitude every 0.87° for $|l| < 60^\circ$, every 1.3° for $30^\circ < |l| < 60^\circ$, and every 4.5° for $60^\circ < |l| < 90^\circ$. In the Outer Galaxy ($|l| > 90^\circ$), we sampled in alternating steps varying from 4.5° to 13.5°. We sampled in Galactic latitude 0.5° and 1.0° above and below the plane at alternate positions in l. In 11 LOSs in the Outer Galaxy with $|l| > 90^\circ$, we sampled $b = \pm 2.0^\circ$ instead of $\pm 0.5^\circ$.

The [C ii] 1.9 THz observations were carried out with the HIFI Band 7b receiver, which is employs Hot Electron Bolometer (HEB) mixers. The HEB bands in HIFI show prominent electrical standing waves that are produced between the HEB mixing element and the first low noise amplifier. The standing wave shape is not a standard sinusoid and is difficult to remove from the resulting spectrum using standard fitting methods (Higgins & Kooi 2009). To remove these standing waves we used a procedure developed at the HIFI Instrument Control Center (ICC; Ian Avruch priv. comm.) which generates a library of standing wave shapes from different observations and finds the best fitting one to correct the observed spectrum (see Higgins 2011 for a detailed description of this method). We processed our data with this standing wave removal script in `HIPE` (Ott et al. 2006) version 8. In `HIPE` we also removed residual standing waves by fitting a single sinusoidal function using the `FitHIFIFringe()` procedure. After all standing waves are removed, we exported our data to the `CLASS90`[2] data analysis software, which we used to combine different polarizations, fit polynomial baselines (typically of order 3), and smooth the data in velocity.

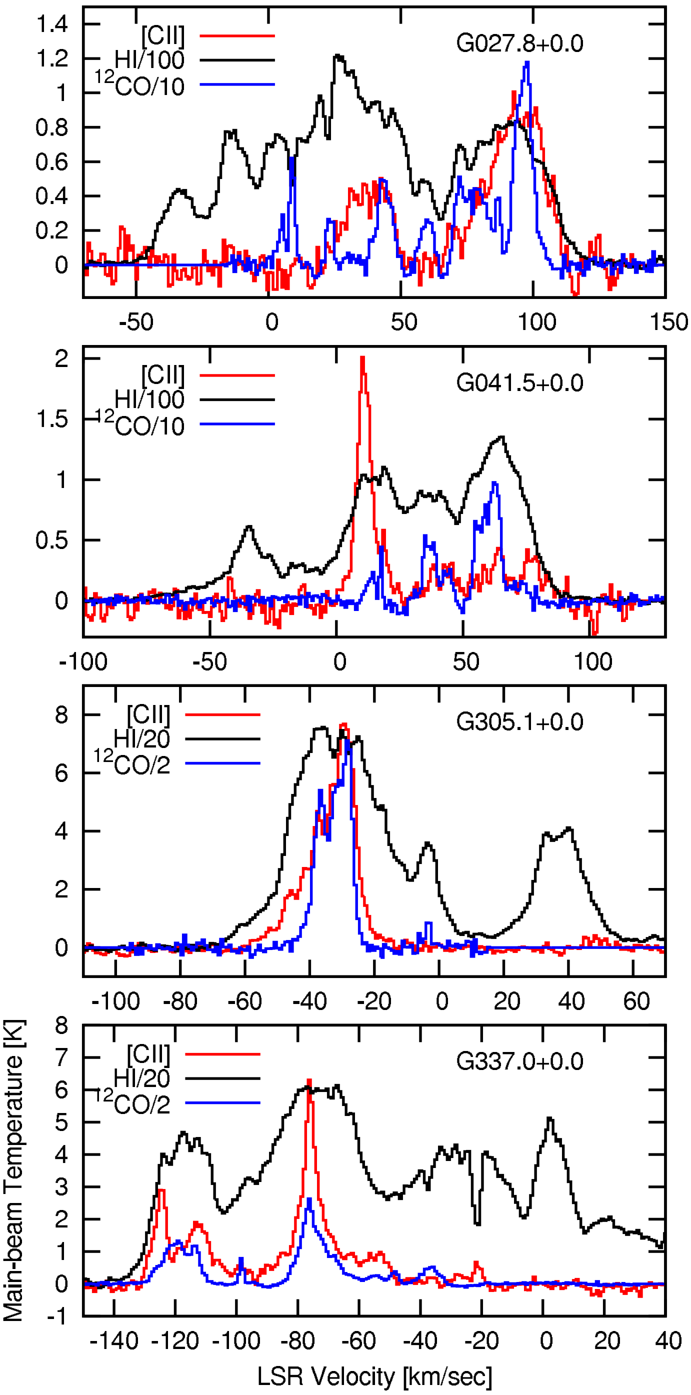

Fig. 1. A selection of GOT C+ lines–of–sight observed in [C ii], H i, and ^{12}CO emission. Note that the [C ii] emission systematically extends closer to the tangent velocity compared with the ^{12}CO line, where it follows the distribution of the H i emission (see Section 3.1).

The angular resolution of the [C ii] observations is $12''$. We applied a main–beam efficiency of 0.72 to transform the data from an antenna temperature to a main-beam temperature scale (Roelfsema et al. 2012).

We used the data produced by the wide band spectrometer (WBS), which have a channel width of 12 MHz (0.16 km s^{-1} at 1.9 THz). We later smoothed the data to a channel width of 0.8

---

[2] http://www.iram.fr/IRAMFR/GILDAS

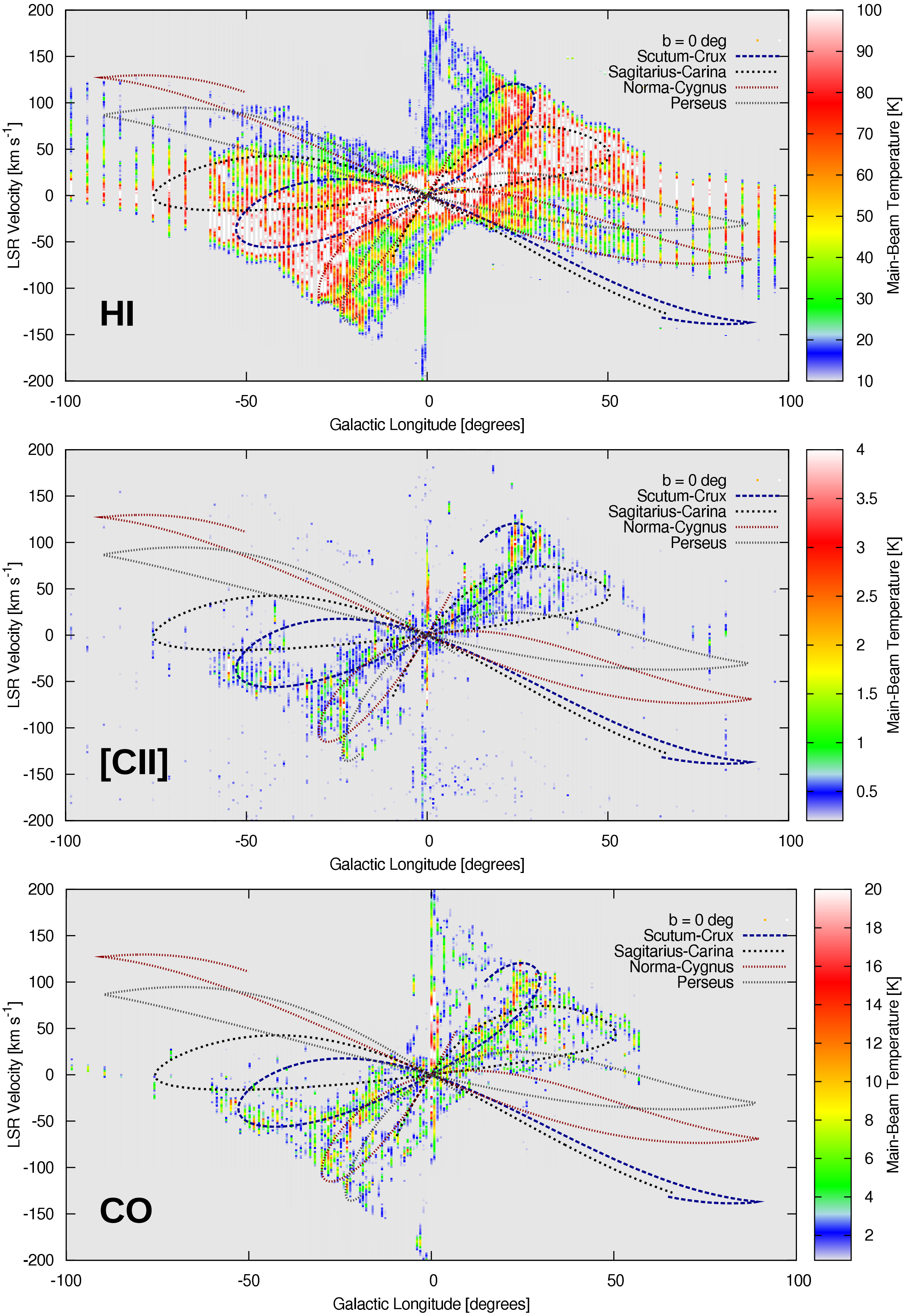

Fig. 2. Position velocity maps of H I, [C II], and ^{12}CO $J = 1 \rightarrow 0$ for the observed GOT C+ LOSs between $l = -100°$ and $100°$ at $b = 0°$. We have overlaid the Scutum-Crux, Sagittarius Carina, Perseus, and Norma-Cygnus spiral arms projected onto the position–velocity maps (see Section 3.1).

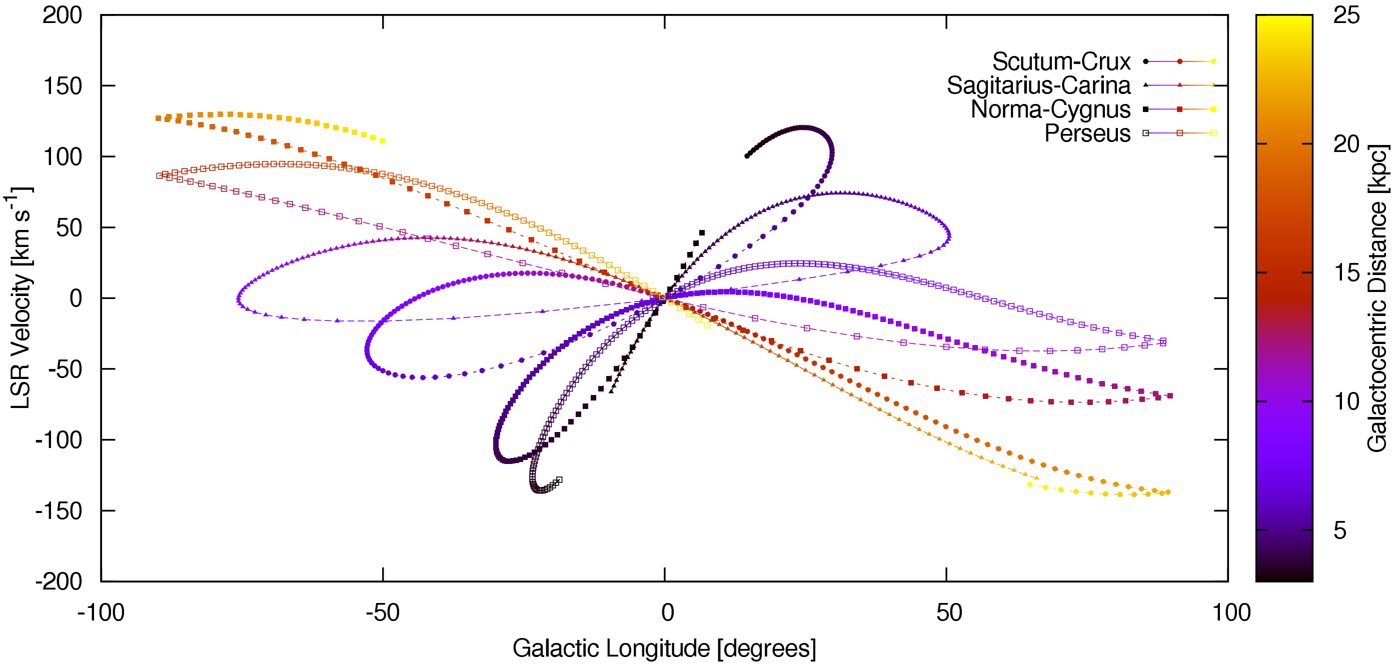

Fig. 3. Projections in the Galactic longitude–velocity map of the Scutum-Crux, Sagittarius Carina, Perseus, and Norma-Cygnus spiral arms (see Section 3.1). The distance to the Galactic center is color coded according to the scale shown at the right.

km s^{-1}. For this channel width the average rms noise of our data is[3] 0.1 K.

As we expected the [C II] emission to be extended in the Galactic plane, we used the LoadChop with reference observing mode. In this observing mode an internal cold calibration source is used as a comparison load to correct short term changes in the instrument behavior. Since the optical path differs between source and internal reference, a residual standing wave structure remains and is corrected with an observation of a sky reference position. For a given Galactic longitude, LOSs with $b = 0°$, $\pm 0.5°$ and $\pm 1.0°$ share the same reference position at $b = \pm 2.0°$. In the 11 Outer Galaxy positions where we observed $b = 0°$, $\pm 1.0°$, and $\pm 2.0°$, we used the $b = \pm 2.0°$ as a reference for $b = 0°$, $\pm 1.0°$ and $b = \pm 4.0°$ as a reference for $b = \pm 2.0°$. We recovered the reference spectrum (OFF) using `HIPE` by subtracting from the ON–OFF spectrum a spectrum for which the reference subtraction step in the HIFI pipeline was suppressed. The resulting spectra include a standing wave with period ∼90 MHz. We combined all observations of the reference spectrum in `CLASS90` and removed the standing wave using a Fast Fourier Transform (FFT) procedure. In the cases where emission in the reference position is present, we decomposed this emission into Gaussian components and corrected the ON–source spectra appropriately. A total of 51% of the GOT C+ spectra were corrected for emission in the reference position.

2.2. CO observations

To complement the GOT C+ data, we observed the $J = 1 \rightarrow 0$ transitions of ^{12}CO, ^{13}CO, and C^{18}O with the ATNF Mopra[4] Telescope. We observed all GOT C+ positions towards the inner Galaxy between $l = -175.5°$and $l = 56.8°$ with an angular resolution of 33′′. Typical system temperatures were 600, 300, and 250 K for ^{12}CO, ^{13}CO, and C^{18}O, respectively. To convert from antenna to main–beam temperature scale, we used a main-beam efficiency of 0.42 (Ladd et al. 2005). All lines were observed simultaneously with the MOPS spectrometer in zoom mode. The spectra were smoothed in velocity to 0.8 km s^{-1} for ^{12}CO and ^{13}CO and to 1.6 km s^{-1} for C^{18}O. The typical rms noise is 0.6 K for ^{12}CO and 0.1 K for both ^{13}CO and C^{18}O. We checked pointing accuracy every 60 minutes using the closest and brightest SiO maser. For $102° < l < 141°$, we used the ^{12}CO $J = 1 \rightarrow 0$ data from the FCRAO Outer Galaxy survey (Heyer et al. 1998). The data have an angular resolution of 45′′, and a rms noise of about 0.6 K in a 0.8 km s^{-1} channel.

2.3. H I data

We used supplementary H I 21 cm data taken from the Southern Galactic Plane Survey (SGPS; McClure-Griffiths et al. 2005), the Canadian Galactic Plane Survey (CGPS; Taylor et al. 2003), and the VLA Galactic Plane Survey (VGPS; Stil et al. 2006). These surveys combined cover the $253° < l < 67°$ portion of the Galactic plane. The SGPS ($253° < l < 358°$) data have an angular resolution of 2′, and a rms noise of 1.6 K per 0.8 km s^{-1} channel. The CGPS covers $74° < l < 147°$, with an angular resolution of 1′, and a rms noise of 2 K in a 0.82 km s^{-1} channel. Finally, the coverage of the VGPS is $18° < l < 67°$, with an angular resolution of 1′, and a rms noise of 2 K in a 0.82 km s^{-1} channel. For the Galactic center we used the data presented by

---

[3] For the typical [C II] FWHM line width of about 3 km s^{-1} (Langer et al. 2013 in preparation), this sensitivity limit corresponds to 1.1×10^{-6} erg s^{-1} cm^{-2} sr^{-1}. The integrated intensity in units of K km s^{-1} can be converted that in units of erg s^{-1} cm^{-2} sr^{-1} using I[K km s^{-1}]=$1.43 \times 10^5 I$[erg s^{-1} cm^{-2} sr^{-1}] (Goldsmith et al. 2012).

[4] The Mopra radio telescope is part of the Australia Telescope which is funded by the Commonwealth of Australia for operation as a National Facility managed by CSIRO.

McClure-Griffiths et al. (2012) which have parameters similar to those of the SGPS. We also used the GALFA–H I Arecibo survey (Peek et al. 2011) to cover the Galactic longitude range between 180°< l <212°. The GALFA–H I data have an angular resolution of 4′ and a typical rms noise of 80 mK in a 1 km s^{-1} channel.

3. The Distribution of [C II] in the Milky Way

3.1. Position–Velocity Maps

In Figure 2 we present the GOT C+ survey in a set of position-velocity maps for $b = 0°$. The corresponding position–velocity maps for ±0.5°, and ±1.0° are presented in Appendix B. The observed [C II] emission peaks at $b = 0°$ and decreases for LOSs above and below the Galactic plane. Most of the [C II] is concentrated in the inner galaxy (−60°≤ l ≤60°). The position–velocity map is overlaid with projections of the Scutum-Crux, Sagittarius-Carina, Perseus, and Norma-Cygnus[5] Milky Way spiral arms. We used the fits to the parameters determining the logarithmic spiral arms presented by Steiman-Cameron et al. (2010) and assumed a flat rotation curve the distance of the Sun to the Galactic center, $R_{\odot} = 8.5$ kpc, and an orbital velocity of the sun with respect to the Galactic center, $V_{\odot} = 220$ km s^{-1}, which are the values recommended by the International Astronomical Union (IAU). We show the projected spiral arms in the range of Galactocentric distance between 3 kpc and 25 kpc. *We can see that most of the [C II] emission is closely associated with the spiral arms and it is brightest at the spiral arms' tangent points*. In Figure 3, we plot the spiral arms with a color scale that represents the Galactocentric distance. Comparing Figure 3 with the panels in Figure 2, we see that the [C II] emission is mostly concentrated within the inner 10 kpc of the Galaxy (see also Section 3.2). The [C II] emission is slightly shifted with respect to that of ^{12}CO, with the [C II] emission present at velocities that are closer to the tangent velocity. This shift can also be seen near the tangent velocities in the sample spectra shown in Figure 1. This suggests that the [C II] emission traces an intermediate phase between the extended H I emission and the cold and dense molecular gas traced by ^{12}CO.

3.2. Radial Distribution Plots

In the following we study the distribution of the [C II] emission as a function of Galactocentric radius. We divided the galaxy in a set of rings with a distance to the Galactic center $R_{\rm gal}$ and width $\Delta R = 0.5$ kpc. For each of these rings, we calculated the azimuthally–averaged integrated intensity per unit length or emissivity of the [C II] line. We describe the procedure used to determine these emissivities in Appendix A.

In Figure 4 we present the azimuthally averaged emissivity of [C II] as a function of Galactocentric radius. The [C II] emission shows a main peak at 4.2 kpc and a secondary peak at ∼ 6 kpc. As mentioned above, the [C II] emission is concentrated in the inner 10 kpc of the Galaxy. When we separate the contribution from LOSs with $l = 0 - 180°$ and $l = 180 - 360°$, we can see that the peak at 4.2 kpc originates from LOSs in the $l = 0 - 180°$ range while the peak at 6 kpc originates from LOSs in the $l = 180 - 360°$ range. This difference in the emissivity distribution between both sides of the Galaxy illustrates the magnitude of the intrinsic scatter within the rings, which is a result of the fact that the Galaxy is not axisymmetric. Because the aim of our analysis is to describe the average properties of the ISM within a Galactocentric ring, we only consider the uncertainties that describe how accurately this azimuthal average emissivity is determined. These uncertainties are generally very small, as they are the result of averaging over a large number of data values. In many figures the error–bars are too small to be visible, especially when the emissivity vary over a large range, and we will quote them in the figure captions. Note that in most cases the uncertainties in the assumptions of our modelling are much larger than those indicated by the observational error–bars.

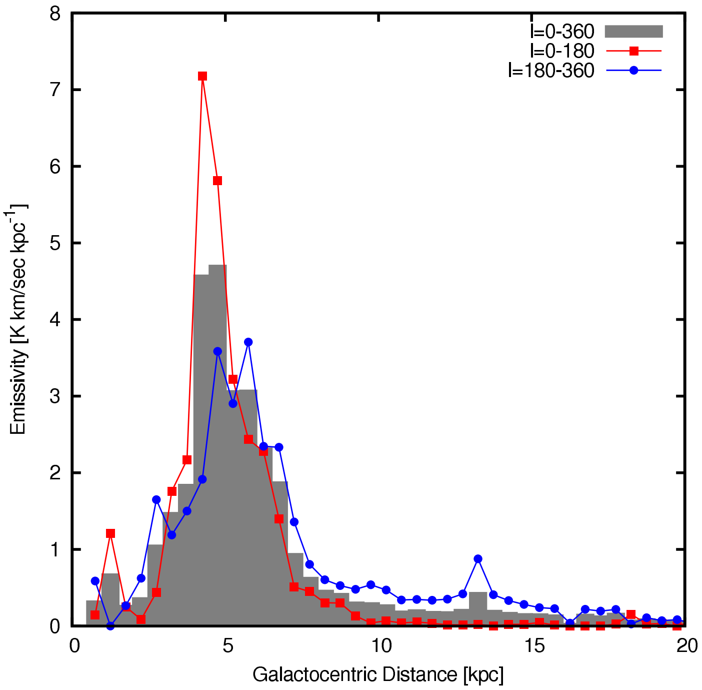

Fig. 4. Radial distribution of the azimuthally averaged [C II] emissivity at $b = 0°$. The shaded area represents the emissivity calculated considering all sampled Galactic longitudes. The connected boxes represent the radial emissivity distribution for 0°< l < 180°, while the connected circles represent that for 180°< l < 360°. The typical 1σ uncertainty in the [C II] emissivity is 0.02 K km s^{-1} kpc^{-1}.

In Figure 5 we show the contributions to the [C II] emissivity from the different spiral arm tangents. We consider LOSs in 12°–wide bins in Galactic longitude centered at the spiral arm tangent locations defined by Vallée (2008). Note that different spiral arms can be seen in this set of LOSs, but the peak of the [C II] emission corresponds to the tangent of the spiral arm. The peak at 4.2 kpc is associated with the Scutum–Crux tangent while the 6 kpc peak is related to the combined emission from the Start of Perseus (peak at 4.7 kpc), Norma-Cygnus (peak at 5.7 kpc), and Crux–Scutum (peak at 6.7 kpc) tangencies. The Sagittarius–Carina (peak at 6.2 kpc) and Carina–Sagittarius (peak at 8.7 kpc) make a smaller contribution. Figure 5 shows that the brightest [C II] emission in the GOT C+ survey arises from the Scutum–Crux tangent at 4.2 kpc.

In Figure 6 we show the radial distribution of the [C II] emissivity from LOSs with $b = 0°$, $b = \pm0.5°$, and $b = \pm1.0°$, and for all observed LOSs together. The [C II] peak at 4.2 kpc from the Scutum-Crux arm is only seen for $b = 0°$, while the intensities from $b = \pm0.5°$, $b = \pm1.0°$ mostly contribute to the intensity at 5.2 kpc from the Galactic center. The shift in the peak of the radial distribution for $|b|$ >0°is related to the vertical struc-

---

[5] The Norma-Cygnus arm is also known as the Norma-3 kpc arm (e.g. Vallée 2008).

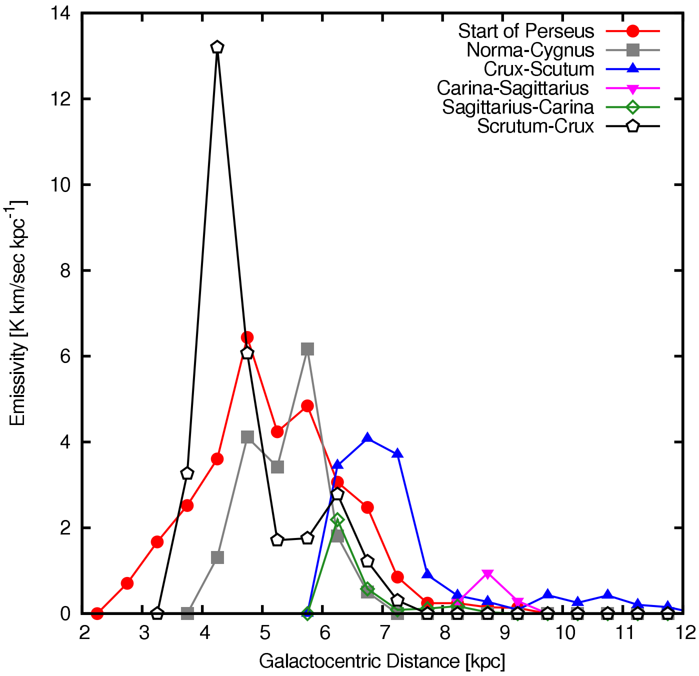

Fig. 5. Radial distribution of the azimuthally averaged [C II] emissivity for GOT C+ LOSs toward the tangents of spiral arms as defined by Vallée (2008).

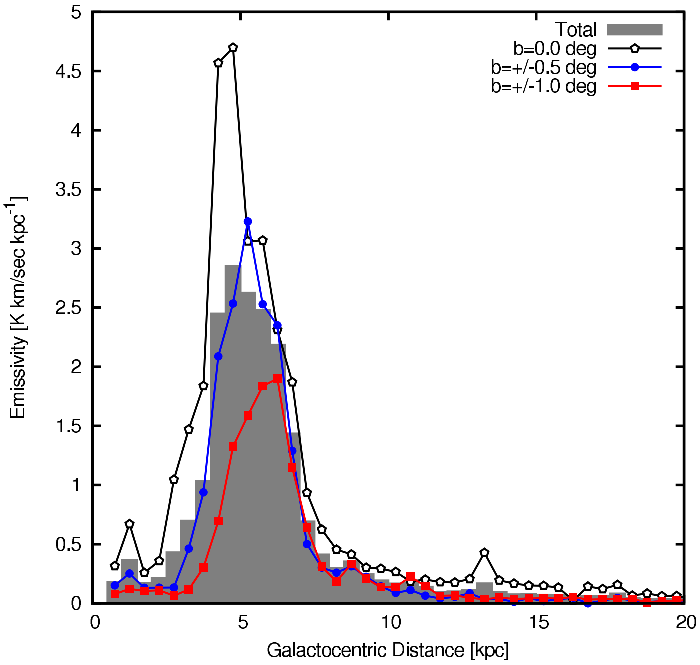

Fig. 6. Radial distribution of the azimuthally averaged [C II] emissivity for LOSs at $b = 0°$, $b = \pm 0.5°$, $b = \pm 1.0°$, and for all observed LOSs together.

ture of the Galactic disk. A cloud with $R_{\rm gal}$ = 5 kpc observed in a LOS with $|b|$=1° would have a vertical distance from the Galactic plane of ∼65 pc, assuming that it is in the near side of the Galaxy, while a cloud with $R_{\rm gal}$ = 4 kpc, in the same situation, would have a vertical distance of ∼100 pc. A Gaussian fit to the latitudinal [C II] distribution observed by BICE (see Fig. 9 in Nakagawa et al. 1998) results in an angular FWHM of the Galactic disk of 1.9°. Assuming that most of their observed [C II] emission is in the near side of the Galaxy at a heliocentric distance of about 4 kpc, this angular FWHM corresponds to 130 pc. Our inability to detect a peak of emission at 4 kpc for $|b| > 0°$ seems to be consistent with this value of the [C II] disk thickness. Results on the vertical structure of the Galactic disk using the GOT C+ data will be presented in a future paper.

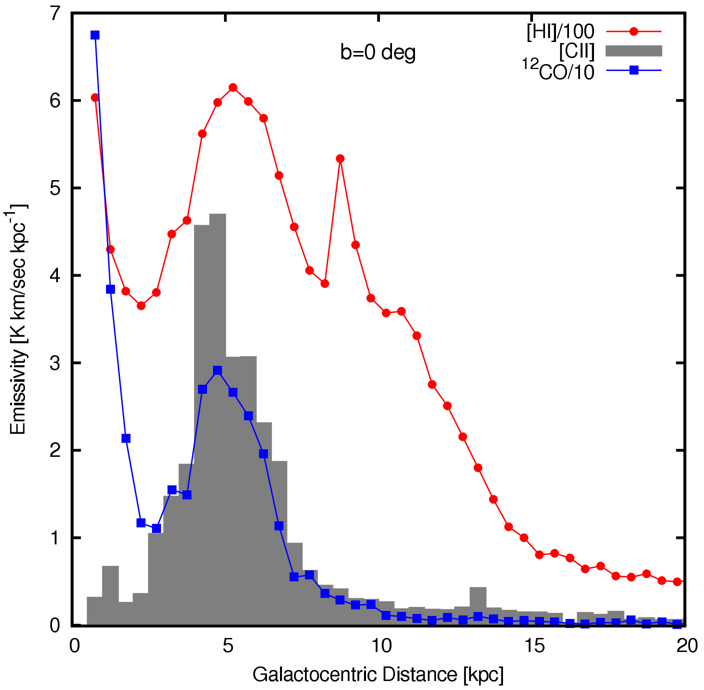

Fig. 7. Radial distribution of the azimuthally averaged [C II], H I, and ^{12}CO emissivities at $b = 0°$. The discontinuity in the H I emissivity distribution at ∼9 kpc is discussed in Section 5.1. Typical 1σ uncertainties in the [C II], H I, and ^{12}CO emissivities (before scaling) are 0.02, 0.6, and 0.1 K km s^{-1} kpc^{-1}, respectively.

In Figure 7, we compare the radial distributions of the [C II], ^{12}CO, and H I emissivities. Typical 1σ uncertainties in the [C II], H I, and ^{12}CO emissivities are 0.02, 0.6, and 0.1 K km s^{-1} kpc^{-1}, respectively. We see that both [C II] and ^{12}CO are mostly concentrated in the 4–10 kpc range, peaking at 4.25 kpc. The distribution of the H I emissivities extends over a larger range of Galactocentric distances, with a peak at 5 kpc.

Table 1. Definition of Mask Regions

Mask	H I	[C II]	^{12}CO	^{13}CO
0	✓	×	×	×
1	✓	×	✓	✓×
2	✓	✓	×	×
3	✓	✓	✓	×
4	✓	✓	✓	✓

✓: Emission is detected in individual spaxels.
×: Emission is not detected.
✓×: Emission is either detected or not detected.

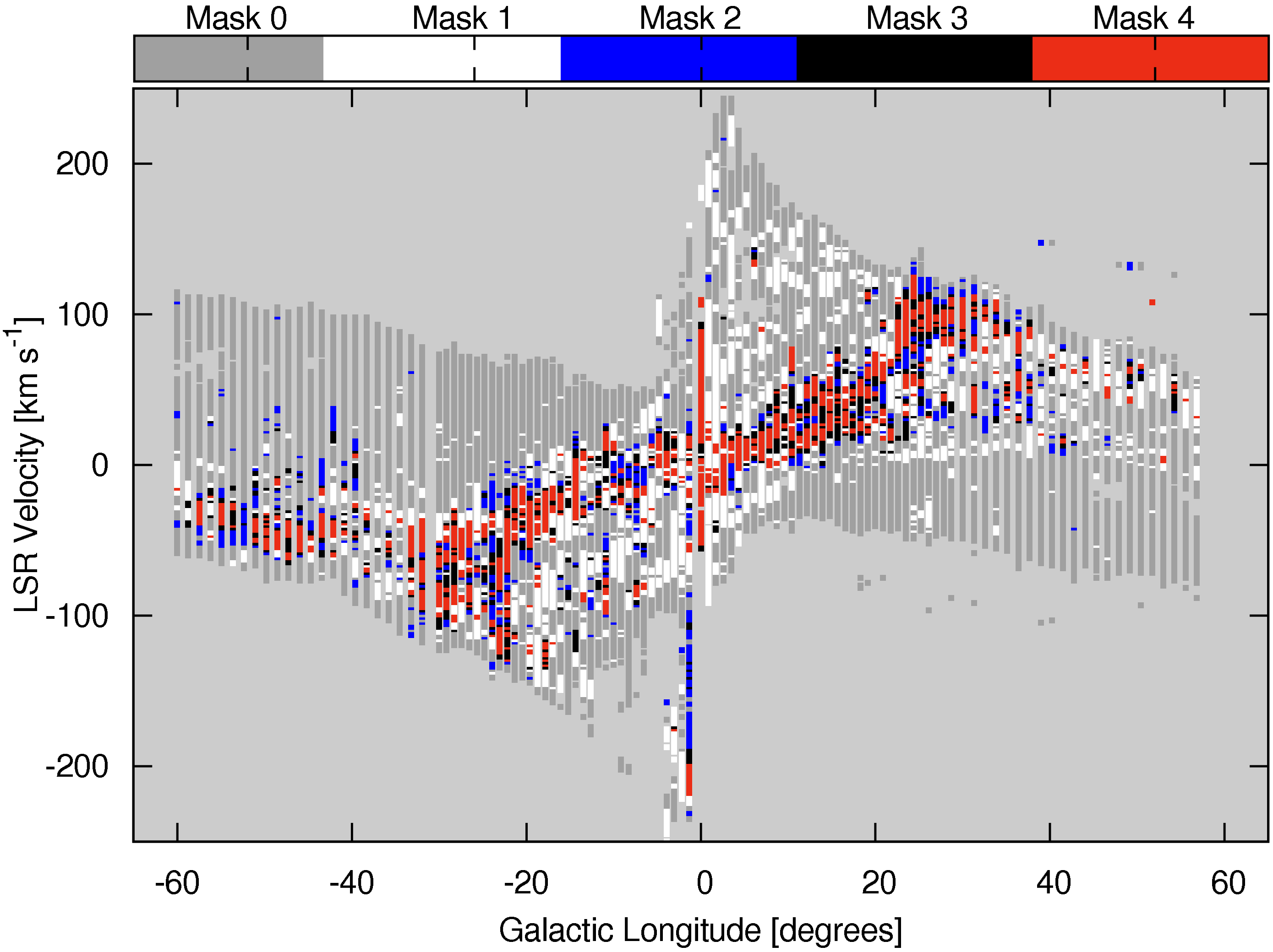

Fig. 8. Position velocity maps of the different types of regions defined in Section 4.1 at $b = 0°$. Mask 0 (*grey*) represents velocity components with only H I detected, Mask 1 (*white*) are components with only H I and CO detected, Mask 2 (*blue*) components with only H I and [C II], Mask 3 (*black*) components with H I, [C II], and CO, and Mask 4 (*red*) components with H I, [C II], ^{12}CO, and ^{13}CO.

4. The origin of the [C II] emission in the Galaxy

4.1. Velocity Components

In the following, we associate the [C II] emission with other tracers in order to separate the contribution from different ISM phases to the observed emission. We define 5 mask regions that represent different stages of the ISM evolution depending whether H I, [C II], ^{12}CO, and ^{13}CO are detected in an individual pixel in the position–velocity map (spaxel). We define Mask 0 as those spaxels in which H I emission is detected but [C II], CO, and ^{13}CO not. These regions likely represent low–volume density atomic gas (see Section 5.1). Mask 1 includes spaxels in which H I and ^{12}CO (or ^{13}CO) are detected but [C II] is not. These spaxels trace dense molecular gas that is too cold for [C II] to be detectable at the sensitivity limit of the observations. Mask 2 are spaxels where H I and [C II] are detected but ^{12}CO is not. These regions are likely larger volume density atomic clouds that have insufficient FUV–photon shielding to allow the build–up of CO and therefore in which most of the gas–phase carbon is in the form of C^{+}. Mask 3 includes spaxels in which H I, [C II], and ^{12}CO are detected but ^{13}CO is not. These regions represent more shielded regions where CO is forming but with inadequate column density to have detectable ^{13}CO emission at the sensitivity of our observations. Finally, Mask 4 includes spaxels in which H I, [C II], ^{12}CO, and ^{13}CO are all detected. These regions likely represent PDRs that have large volume and column densities and are warm enough to produce significant [C II] emission. In Table 1 we present a summary of the Mask region definitions.

In Figure 8 we present the distribution of the different Masks in the position–velocity map of the Galaxy for $-60° < l < 60°$ and $b = 0°$. We present similar position–velocity maps for $b = \pm0.5°$ and $\pm1.0°$ in Appendix B (Figure B.5). The dense PDRs (Mask 4) are closely associated with the spiral arms. These regions are surrounded with spaxels in Mask 3 which, in turn, are surrounded with spaxels in Mask 2. We suggest that this spatial arrangement indicates that Mask 3 and Mask 2 represent the envelopes of the active star–forming regions traced by Mask 4. There is a significant fraction of spaxels in Mask 1, particularly in the molecular ring and local arms. Mask 0 represents the largest fraction of spaxels.

Figure 9 presents the intensity distribution of H I, [C II], ^{12}CO, and ^{13}CO for the different Mask regions defined above for $b = 0°$. Although by definition Masks 0 and 1 have no [C II] emission in a given spaxel, its emission can still be seen when the

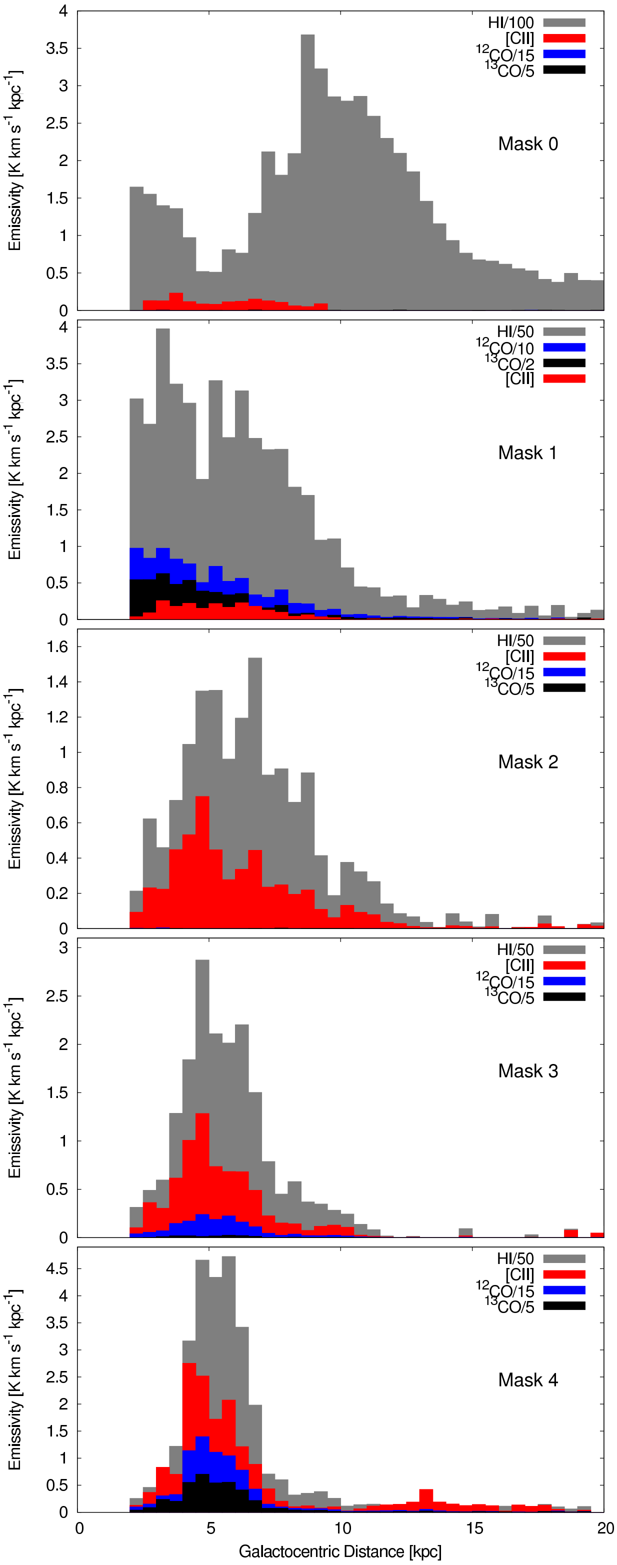

Fig. 9. Galactocentric distribution of the different types of regions defined in Section 4.1. The plots include data from all LOSs at $b = 0^\circ$, $b = \pm0.5^\circ$, and $b = \pm1.0^\circ$.

data is averaged over the different rings. The same result happens with ^{13}CO in Mask 3. The detection of emission after averaging the data in azimuth shows that our classification into Masks depends on the sensitivity of our observations. We will study the [C II] emission in Mask 0 and 1 and the ^{13}CO emission in Mask 3 separately as they represent a different population of clouds that are weak in [C II] and ^{13}CO, respectively.

4.2. Atomic gas

We first assumed that all the observed [C II] emission arises from a purely atomic gas at a kinetic temperature $T_{\rm kin} = 100$ K. For optically thin emission, the [C II] intensity (in units of K km s^{-1}) is related to the C$^+$ column density, N_{C^+} (cm^{-2}), and volume density of the collisional partner, n (e$^-$, H, or H$_2$; cm^{-3}), as (see e.g. Goldsmith et al. 2012),

$$I_{\rm [CII]} = N_{\rm C^+}\left[3.05\times10^{15}\left(1+0.5\left(1+\frac{A_{ul}}{R_{ul}n}\right)e^{91.21/T_{\rm kin}}\right)\right]^{-1}, \quad (1)$$

where $A_{\rm ul} = 2.3\times10^{-6}$ s^{-1} is the Einstein spontaneous decay rate and R_{ul} is the collisional de–excitation rate coefficient at a kinetic temperature $T_{\rm kin}$. We used a value of R_{ul} for collisions with H at $T_{\rm kin} = 100$ K of 8.1×10^{-10} s^{-1} cm^{-3} (Launay & Roueff 1977). In the optically thin limit we can estimate the atomic gas column density, N(H), from the H I 21 cm observations using, $N({\rm H}) = 1.82\times10^{18} I({\rm HI})$ cm^{-2}, with I(HI) in units of K km s^{-1}. Observations of H I absorption toward continuum sources, however, suggest that the opacity of H I increases toward the inner Galaxy, where the assumption of optically thin emission might not apply. Kolpak et al. (2002) derived an average value, assuming $T_{\rm kin} = 50$ K, of $\tau \simeq 1$ for $R_{\rm gal} < 8.5$ kpc. For our assumed $T_{\rm kin} = 100$ K, this opacity corresponds to $\tau \simeq 0.5$. We used this opacity to correct the H I column densities derived from the 21 cm line that is associated with [C II] emission, resulting in a 30% increase in the derived column density.

The column density of ionized carbon can be estimated from N(H I) assuming an appropriate [C]/[H] fractional abundance, provided that all gas–phase carbon is in the form of C$^+$. There is evidence that the gas–phase abundance of metals in the Milky Way decreases with Galactocentric distance. Rolleston et al. (2000) found that the fractional abundance distribution of several light elements (C, O, Mg & Si) can be represented by a linear function with slope -0.07 ± 0.01 dex kpc^{-1} over 6 kpc $< R_{\rm gal} <$ 18 kpc . We use this relationship to convert N(H) to N(C$^+$) for any given galactocentric distance, assuming that the slope of the relative abundance gradient does not change significantly for $R_{\rm gal} <$ 6 kpc. We assume a [C]/[H] fractional abundance of 1.4×10^{-4} for $R_{\rm gal} = 8.5$ kpc (Cardelli et al. 1996). The [C]/[H] abundance as a function of Galactocentric distance is thus given by

$$[{\rm C}]/[{\rm H}] = 5.5\times10^{-4}10^{-0.07R_{\rm gal}}. \quad (2)$$

The [C]/[H] abundance drops by a factor of 2.6 from $R_{\rm gal} = 4$ kpc to 10 kpc.

With the estimated value of $N(C^+)$ we used Equation (1) to solve for the volume density of H I that is required to match the observed [C II] emission, under the assumption that all observed [C II] emission comes from atomic gas. In Figure 10a, we present the distribution of hydrogen volume densities as a function of Galactocentric distance for the different Mask regions for 4 kpc $< R_{\rm gal} <$ 11 kpc, which is the range of $R_{\rm gal}$ in which most of the [C II] emission is detected. The H volume density increases toward the Galactic center with a range between 100 cm^{-3} to 10^3 cm^{-3} for Masks 2, 3 and 4. For Masks 0 and 1 the volume densities are more moderate, ranging from 20 to 80 cm^{-3}. In Figure 10b, we present the corresponding thermal pressures ($p/k = nT_{\rm kin}$) as a function of Galactocentric distance for the

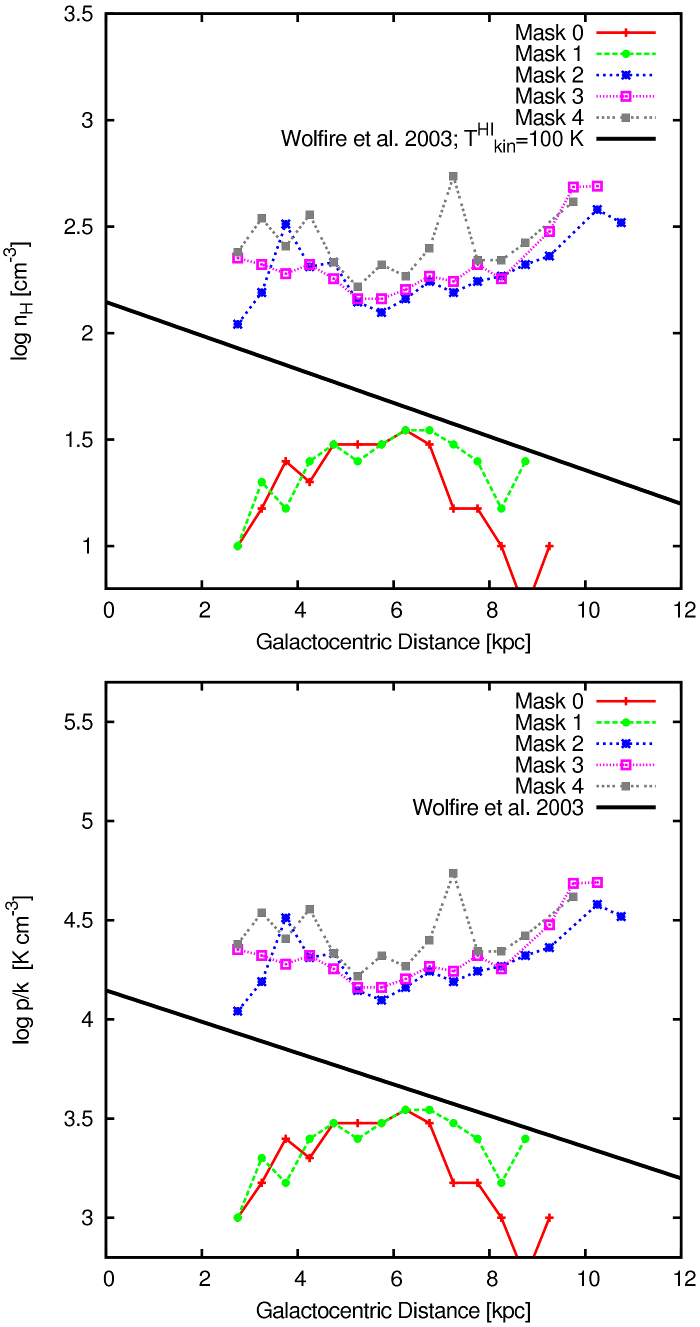

Fig. 10. (*Upper panel*) Neutral hydrogen volume density as a function of Galactocentric distance for the Mask regions defined in Section 4.1, assuming that all [C II] is associated with atomic gas at $T_{\rm kin} = 100$ K. (*Lower panel*) Corresponding thermal pressure as a function of Galactocentric distance.

different Mask regions. We also show the thermal pressure distribution suggested by Wolfire et al. (2003),

$$p/k = 1.4 \times 10^4 \exp\left(\frac{-R_{\rm gal}}{5.5\,{\rm kpc}}\right) {\rm K\,cm^{-3}}, \qquad (3)$$

corresponding to the predicted thermal pressure of the CNM gas. Masks 0 and 1 have thermal pressures that are consistent with those suggested by Wolfire et al. (2003). Thus, the densities and thermal pressures estimated in Masks 0 and 1 are consistent with their [C II] emission originating from the CNM. Masks 2, 3, and 4 have volume densities and thermal pressures that are about one order of magnitude larger than those observed and predicted for the CNM. We therefore conclude that the assumption that the [C II] emission in Masks 2, 3, and 4 originates entirely from atomic gas is incompatible with our observations. As we will discuss below, part of the observed [C II] emission in Masks 2, 3, and 4 also emerges from molecular, and to a lesser extent, from ionized gas.

Motivated by the agreement between the pressures derived in Masks 0 and 1 and those predicted in Equation (3), we used this expression to estimate, assuming a constant $T_{\rm kin} = 100$ K, the radial H volume density distribution the atomic gas associated with Masks 2, 3, and 4. We then used Equation (1) to estimate the contribution from CNM gas to the observed [C II] emission in these Mask regions. Note that for a given thermal pressure, the intensity of [C II] associated with H I has a only weak dependence on the assumed kinetic temperature, varying by about ±20% in the range between 60 and 200 K.

In Figure 11 we show the resulting contribution from atomic gas to the [C II] intensity as a function of the Galactocentric distance. We estimate that the contribution from [C II] emerging from the atomic gas component represents 21% of the observed intensity.

4.3. Ionized gas

It has been suggested that a significant fraction of the [C II] emission in the Galaxy observed by COBE emerges from the Extended Low Density Warm Ionized Medium (ELDWIM; Petuchowski & Bennett 1993; Heiles 1994). We estimated the contribution to the observed [C II] emission from an ionized gas using the Galactic distribution of the electron density used by the NE2001 code (Cordes & Lazio 2002). The NE2001 code assumes a Galactic distribution of the electron density, including a thin and thick disk, spiral arms (four), and Galactic center components. This electron density distribution is further constrained using observations of the dispersion measure of pulsars.

We used the NE2001 model to extract the electron density as a function of heliocentric distance for all GOT C+ lines–of–sight in the Galactic plane. For each step in heliocentric distance we also calculate the column density of electrons and, assuming the [C]/[H] gradient (Equation 2), the column density of C$^+$ associated with the ionized gas. We estimate the [C II] intensity as a function of heliocentric distance for each line–of–sight using Equation (1), assuming a kinetic temperature of 10^4 K, and excitation by collisions with electrons ($R_{ul} = 4.8 \times 10^{-8}$ s^{-1} cm^{-3}; Wilson & Bell 2002). The term involving the kinetic temperature in Equation (1) becomes unity for such a large temperature, therefore the intensity of [C II] associated with ionized gas is insensitive to the kinetic temperature. Note that the NE2001 model is smooth and can only reproduce the electron density distribution over large scales. Finally, we calculated the distribution of the [C II] emissivity as a function of Galactocentric distance taking the same considerations as described in Appendix A. The resulting radial distribution is shown in Figure 11. We estimated that the contribution from [C II] arising from ionized gas represents only 4% of the total observed intensity.

Velusamy et al. (2013) observed an excess of [C II] emission at the tangent velocities towards the Scrutum–Crux spiral arms tangent which was interpreted as coming from compressed ionized gas. They suggested that this compression of ionized gas is the result of the passing of a spiral arm density wave. Note, however, that this excess can only be detected toward spiral arm tangencies due to a projection effect by which the path length toward a spiral arm is maximized. We therefore do not expect a significant contribution from this excess to the overall observed [C ii] intensity.

Note that our estimation of the contribution from ionized gas to the observed [C ii] emission corresponds only to that for lines–of–sight in the Galactic plane with b=0°. The ELDWIM gas is known to have a scale height of about 1 kpc (Kulkarni & Heiles 1987; Reynolds 1989), which is much larger than that of the atomic and molecular gas ($\sim$ 100 – 300 pc). Thus, the contribution from ionized gas to the total [C ii] *luminosity* of the Galaxy should be larger than what is suggested by the emissivities at $b = 0°$. At a distance from the Sun of 4 kpc, a 1 kpc scale height corresponds to 14°. Thus, within the a 7° beam of COBE, the [C ii] emission from the ionized component fills the beam, while the emission from the Galactic plane (vertical angular scale $\sim$2 deg; Nakagawa et al. 1998) will be significantly beam diluted. The [C ii] emission from the Galactic plane and that from the extended ionized medium should appear comparable within a COBE beam, as suggested by several analyses (Petuchowski & Bennett 1993; Heiles 1994). A detailed analysis of the relationship between the *Herschel*/HIFI [C ii] observations and those from COBE/FIRAS will be presented in a future paper.

4.4. Dense photon-dominated regions

It is possible that a significant fraction of the observed [C ii] intensity in the Galactic plane comes from dense PDRs, as observations of Galactic and extragalactic PDRs have shown that they are the sources of bright [C ii] emission (e.g. Stacey et al. 1991; Boreiko et al. 1988). Note that the main–beam temperatures in the GOT C+ survey are mostly in the 0.5–8 K range, with only a few spaxels with $T_{\rm mb} > 8$ K (see Fig. 7 in Goldsmith et al. 2012). This range of main beam temperatures is well below that observed in nearby star–forming regions such as Orion ($\sim$100 K) which are powered by the intense FUV radiation field produced by nearby massive stars. Bright PDRs are, however, not numerous enough to dominate the global [C ii] emission in the Milky Way. In Section 6 (see also Pineda et al. 2010a) we found that most of the [C ii] emission in the Galactic plane arises from regions which are exposed to moderate–strength FUV fields, in agreement with models of the Galaxy based on COBE data (Cubick et al. 2008). We considered [C ii] velocity components associated with ^{13}CO (Mask 4) as likely to be associated with dense and warm PDRs. Such regions have large enough column densities, and presumably sufficient volume densities, to produce detectable ^{13}CO emission while they are also warm enough to produce detectable [C ii] emission. We determined the contribution from dense PDRs to the observed [C ii] intensity in Mask 4 by subtracting the [C ii] emission associated with atomic gas, as determined in Section 4.2. The resulting radial distribution of the [C ii] emissivity associated with dense PDRs is shown as a red-dashed line in Figure 11. The [C ii] emission emerging from dense PDRs represents 47% of the total emission observed in the GOT C+ survey.

4.5. [C ii] Excess

The combined contribution to the [C ii] emission from atomic gas, ionized gas, and dense PDRs, as estimated above, can account for only 72% of the observed emission. It has been suggested the remaining [C ii] emission is produced in the envelopes of dense molecular clouds where the H i/H_2 transition is largely complete, but the column densities are low enough that the C^+/C^0/CO transition is not (e.g Madden et al. 1997; Langer et al. 2010). Since this H_2 gas component is not traced by CO, but by [C ii] and to a lesser extent by [C i], we refer to it as “CO–dark H_2 gas”. In the following section we derive the distribution of the CO–dark H_2 gas in the plane of the Milky Way, and compare it to that traced by ^{12}CO and ^{13}CO.

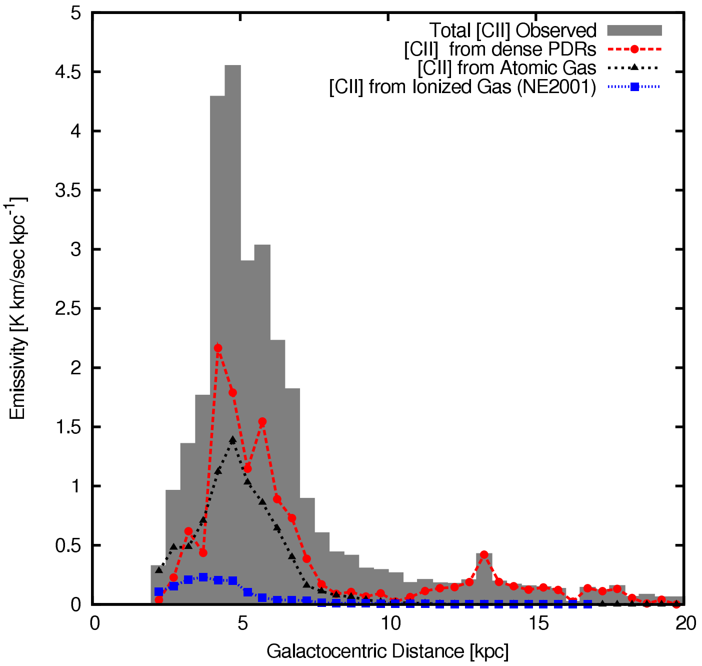

Fig. 11. Azimuthally–averaged radial distribution of the observed [C ii] emissivity in Masks 2, 3, and 4 together with the different contributions from the ISM components discussed in Section 4. Typical uncertainties are 0.02 K km s^{-1} kpc^{-1} for the total [C ii] emission and that contributed from dense PDRs, and 0.001 K km s^{-1} kpc^{-1} for the contribution from H i gas. For the contribution from ionized gas, we assume 30% uncertainties or 0.07 K km s^{-1} kpc^{-1}.

5. The distribution of the ISM components in the plane of the Milky Way

5.1. The Warm and Cold Neutral Medium

As mentioned earlier, atomic gas is predicted to be in two phases in roughly thermal pressure equilibrium, the Cold Neutral Medium (CNM; $n_{\rm H} \simeq 50\,{\rm cm}^{-3}$; $T_{\rm kin} \simeq 80$ K) and the Warm Neutral Medium (WNM; $n_{\rm H} \simeq 0.5\,{\rm cm}^{-3}$; $T_{\rm kin} \simeq 8000$ K). Because atomic hydrogen is one of the main collisional partners of C^+, the [C ii] line is a tracer of atomic gas that has the advantage over the 21 cm line (observed in emission) that it is sensitive to both the volume density and the kinetic temperature of the gas (Equation 1). Thus, the [C ii] line should in principle trace both the WNM and CNM atomic gas components. In practice, however, because of the volume density contrast between the CNM and WNM, the [C ii] line is expected to be significantly weaker for WNM gas compared to the emission from CNM gas (Wolfire et al. 2010). For the H i peak intensity of 160K (in a 0.8 km s^{-1} channel width) at the 5 kpc ring, and considering the abundance and thermal pressure gradients (Equation 2 and 3, respectively), we can use Equation (1), assuming 100 K for the CNM and 8000 K for the WNM, to estimate a [C ii] intensity associated with H i of 0.3K in the case that all gas is CNM, and of

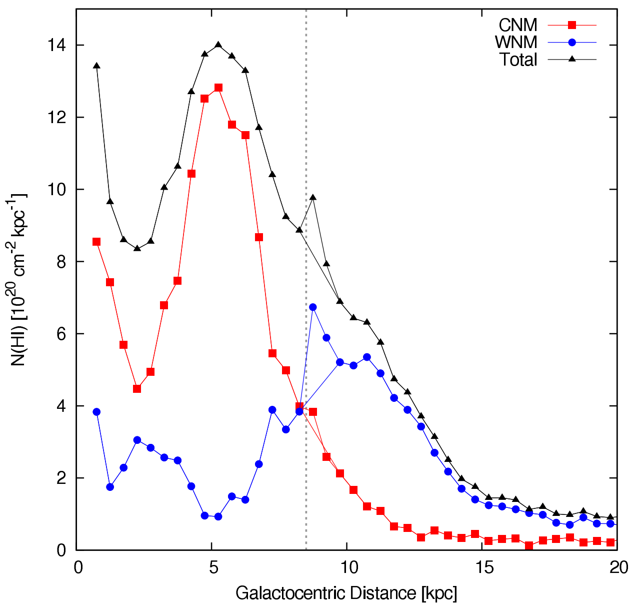

Fig. 12. Radial distribution of the azimuthally averaged total H i column density in the Galactic plane. We also include the estimated radial distribution of the cold neutral medium (CNM) and warm neutral medium (WNM) gas. Typical uncertainties of the H i column densities are 10^{18} cm^{-2} kpc^{-1}. The vertical line shows the Solar radius. At 9 kpc there is a discontinuity in the total and WNM N(H i) distribution which is attributed to the abrupt change between the number of rings sampled in the inner and outer Galaxy. We therefore also show lines that smoothly connect the distributions in the inner and outer Galaxy.

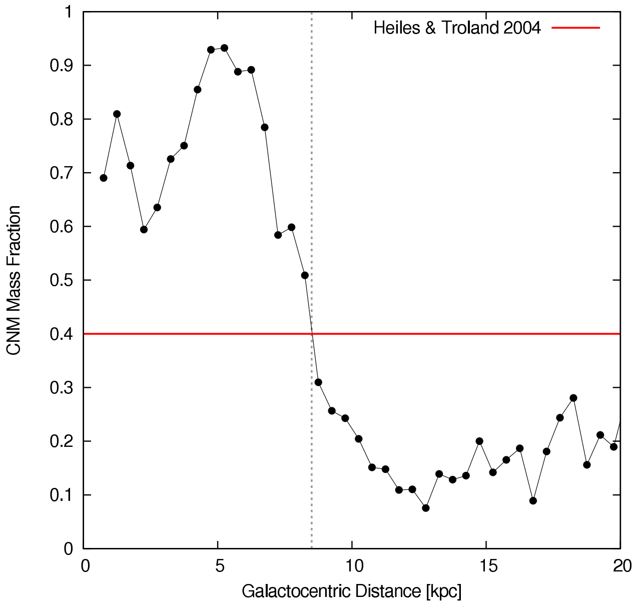

Fig. 13. Radial distribution of the mass fraction of the atomic gas in the cold neutral medium (CNM). The horizontal line shows the local mass fraction of the CNM derived by Heiles & Troland (2003). The vertical line denotes the solar radius. The typical uncertainty in the ratio is ~0.002.

0.04K in case all gas is WNM. Considering our 3σ sensitivity limit per channel of 0.3 K we find that weak CNM gas can be detected, while WNM gas would be too weak to be detected in individual spaxels.

When azimuthally averaging (Section 4.2), however, [C ii] emission associated with CNM can produce a significant contribution to the observed [C ii] emissivity. For the $R_{\rm gal}$ = 5 kpc peak of 1.4×10^{21} cm^{-2} kpc^{-1}, we find a contribution of 1.1 K km s^{-1} kpc^{-1} for all H i gas in CNM, and 0.04 K km s^{-1} kpc^{-1} for all H i gas in WNM. As the 3σ sensitivity limit for the azimuthal average is 0.06 K km s^{-1} kpc^{-1} (Appendix A), we see that WNM is always below the sensitivity limit even for the azimuthal average. This suggests that only the CNM can contribute to the observed [C ii] emission. We therefore assume that spaxels that have both H i and [C ii] emission (Masks 2, 3, and 4) are associated with CNM gas. In our survey, there are also spaxels where H i and ^{12}CO emission are detected but [C ii] emission is not (Mask 1). These regions are likely too cold and/or have too low volume densities for [C ii] to be detected, but can still be associated with cold H i gas. We therefore also consider H i associated with Mask 1 as being in the CNM phase. Finally, we consider spaxels with H i but neither [C ii] nor ^{12}CO emission (Mask 0) to be associated with WNM gas. In the following we use this criteria to separate the CNM and WNM components from the observed H i emission and study their distribution in the plane of the Milky Way.

It is possible that some spaxels have [C ii] emission that is below the sensitivity limit for individual spaxels but can still be detected in the azimuthal average. In Figure 9, we see that [C ii] emission (~0.1 K km s^{-1} kpc^{-1}) in the inner galaxy can be detected in the region where only H i is detected in the pointed observations (Mask 0). The average H i column for $R_{\rm gal}$ = 3 – 8 kpc (~ 1×10^{20} cm^{-2} kpc^{-1}), would imply a [C ii] emissivity of about 0.17 K km s^{-1} kpc^{-1} in the case that all gas is CNM and 0.006 K km s^{-1} kpc^{-1} in the case that all gas is WNM. Thus, the emission detected in Mask 0 can only be associated with CNM gas. Note that for the inner galaxy, when we associate H i with [C ii] and/or ^{12}CO emission in individual spaxels, we are assuming that the H i and [C ii] and/or ^{12}CO emission arises from both the near and far side of the Galaxy. We could in principle overestimate the H i column density associated with the CNM in the case that the [C ii] and/or ^{12}CO emission arises from either the near or far side of the galaxy, but H i from both sides. We consider this situation unlikely, however, as we expect that the physical conditions within a galactocentric ring to be relatively uniform. The maximum effect, in the case that all LOSs in the inner galaxy are affected, is a reduction of the azimuthally averaged CNM column density by a factor of ~2 (and a corresponding increase of the WNM column density by the same factor).

In Figure 12, we show the radial distribution of the total H i column density together with that of the contributions from CNM and WNM gas. The column densities are estimated from the H i emissivity distributions which are in turn calculated considering all spaxels with H i emission as well as those associated with CNM gas (Masks 1, 2, 3, and 4) and those associated with WNM gas (Mask 0). The column density of CNM gas was corrected for opacity effects as described in Section 4.2. The value of N(H i) at $R_{\rm gal}$ = 8.5 kpc (6.7×10^{20} cm^{-2} kpc^{-1}; without the opacity correction) is in good agreement with the local value of the H i surface density of 6.2×10^{20} cm^{-2} found by Dickey & Lockman (1990). As we can see, the CNM dominates the H i column density in the inner Galaxy, while WNM dominates in the outer Galaxy. The column density of the WNM gas in the inner Galaxy is similar to what we estimated for the H i column density required to reproduce the [C ii] emission resulting from the azimuthal average in Mask 0. This result indicates that even a larger fraction of the atomic gas in the inner Galaxy might be in the form of CNM. CNM clouds may still exist in the outer Galaxy, as molecular clouds and star formation are present, and the reduction of its contribution in the outer Galaxy might be a result of a reduced filling factor of the CNM gas.

There is a discontinuity in the total H I column density distribution at around 9 kpc, which may be an artifact of the assumed flat rotation curve with purely circular motions. An alternative explanation is shown in Figure A.2 in Appendix A, which shows the number of ring samples as a function of Galactocentric distance. Because a LOS samples a ring in the inner Galaxy twice but a ring in the outer Galaxy only once, there is a discontinuity in the number of samples between the inner and outer Galaxy. This discontinuity will therefore affect the azimuthally averaged emissivity distributions. The effect on the [C II] and ^{12}CO emissivity distributions is small because it coincides with a steep decrease in the value of the sum of the emissivities for each sample (see numerator in Equation A.8). In the case of H I, however, the sum of the emissivities for each sample is smooth at around 9 kpc, and therefore dividing by the number of samples results in a noticeable discontinuity. In Figure 12, we also show the H I column density distribution where data points with $R_{\rm gal} < 9$ kpc and $R_{\rm gal} > 11$ kpc are smoothly connected.

In Figure 13 we present the mass fraction of the CNM gas. In the inner Galaxy, up to 90% of the atomic gas is in the form of CNM, with even a larger percentage being possible based on the discussion above. For larger Galactocentric distances, this fraction decreases to only 0.1–0.2, showing little variation with Galactocentric distance. These results are in good agreement with those found by Dickey et al. (2009) using H I emission/absorption observations in the outer Galaxy. At $R_{\rm gal} = 8.5$ kpc, we find that the fraction is in good agreement with the local fraction of 0.4 derived by Heiles & Troland (2003). We derive an average CNM mass fraction for the entire Galactic disk of 0.43.

Our results suggest that the CNM is the dominant atomic gas phase in the inner Galaxy while the WNM dominates the outer Galaxy. The increase of the fraction of CNM gas towards the inner Galaxy coincides with that of the ^{12}CO and [C II] emissivities. This suggests that the CNM plays a important role as the precursor of molecular clouds that will eventually form stars.

5.2. Molecular Hydrogen

5.2.1. CO–dark H_2 gas

To derive the column density radial distribution of the CO–dark H_2 gas component, we first estimated the C^+ column density associated with the [C II] excess emission derived in Section 4. The C^+ column density, which can be derived by inverting Equation (1), depends on the observed [C II] intensity, the H_2 volume density, $n_{\rm H_2}$, and the kinetic temperature of the H_2 gas, $T_{\rm kin}^{\rm H_2}$. Without an independent estimate of the physical conditions in the CO–dark H_2 layer, we need to make an assumption about the value of $n_{\rm H_2}$ and $T_{\rm kin}^{\rm H_2}$. In Section 4.2, we derived the contribution from atomic gas (CNM) to the observed [C II] intensity by estimating the H I volume density, $n_{\rm HI}$, from the radial thermal pressure distribution (Equation 3), assuming a kinetic temperature of the H I gas, $T_{\rm kin}^{\rm HI}$, of 100 K. After the H/H_2 transition takes place, and as the column density increases, self–gravity starts to become important, resulting in a gradual increase of the volume density of the gas. The increased shielding of FUV photons results in a decreased gas heating, while line cooling is largely unaffected due to the larger volume densities, resulting in a reduction of the kinetic temperature. Overall, however, the thermal pressure of the gas increases with column density: studies of local clouds, in CO absorption in the millimeter (Liszt & Lucas 1998) and in the UV (Goldsmith 2013 submitted), tracing column densities up to that of the C^+/C^0/CO transition layer, typically suggest thermal pressures in the range between 10^2 to 10^4 K cm^{-3}, while for well shielded regions, traced by ^{13}CO, excitation studies suggest thermal pressures in the range between 10^4 to 10^5 K cm^{-3} (Sanders et al. 1993). It is therefore likely that a thermal pressure gradient is present in the region between the H/H_2 and C^+/C^0/CO transition layers, where the emission from CO–dark H_2 gas originates. To estimate the

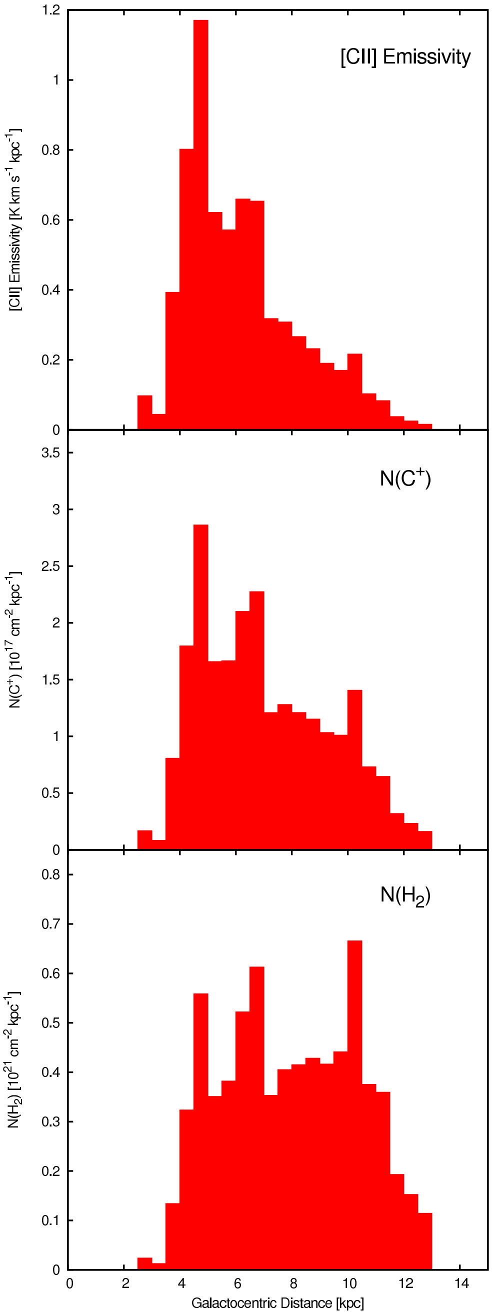

Fig. 14. Radial distribution of the azimuthally averaged excess [C II] emissivity as discussed in Section 4.5 (*upper panel*). Radial distribution of the C^+ column density derived from the excess [C II] emissivity (*middle panel*). Radial distribution of the H_2 column densities derived from $N(C^+)$ associated with the excess [C II] emissivity (*lower pannel*).

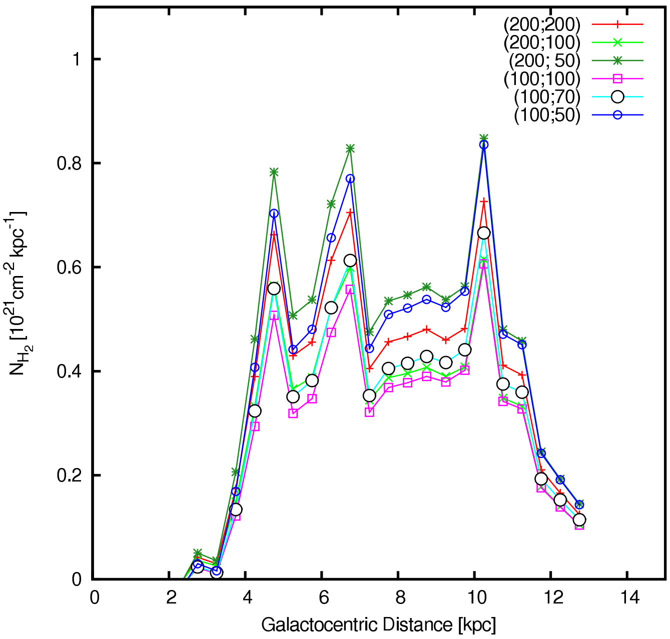

Fig. 15. CO–dark H_2 gas column density as a function of Galactocentric distance for different H ɪ and H_2 temperature pairs ($T^{\rm HI}_{\rm kin}$;$T^{\rm H_2}_{\rm kin}$). The corresponding volume densities were derived from Equation (3; see Section 5.2.1).

column density of CO-dark H_2 gas, we assume that the thermal pressure of the CO–dark H_2 gas is the geometric mean between that of the H ɪ gas (Equation 3) and the maximum observed at the C^+/C^0/CO transition layer. At the solar neighborhood, the minimum pressure given by Equation 3 is 3000 K cm^{-3} while the maximum pressure at the C^+/C^0/CO transition layer given by Goldsmith (2013) is 7400 K cm^{-3}. The resulting geometric mean is 4700 K cm^{-3}, which is a factor of 1.6 larger than the thermal pressure given by Equation (3). We therefore multiply Equation (3) by this factor to determine the mean thermal pressure of the CO–dark H_2 gas as a function of Galactocentric distance. We assume a constant kinetic temperature of $T^{\rm H_2}_{\rm kin}$=70 K, following the results from Rachford et al. (2002), and a corresponding R_{ul} = 4.3×10^{-10} s^{-1} cm^{-3} (Flower & Launay 1977) for collisions with H_2. Using this kinetic temperature we derive the H_2 volume density of the CO–dark H_2 gas from Equation (3) as discussed above. We will discuss below the effects of choosing different values of $T^{\rm H_2}_{\rm kin}$ and $n(H_2)$ in the derivation of the column density of the CO–dark H_2 gas. We finally converted the radial distribution of the C^+ column density to that of the H_2 column density, assuming that all gas–phase carbon is in the form of C^+, by applying a [C]/[H_2] abundance gradient. The [C]/[H_2] abundance ratio is twice the [C]/[H] ratio given in Equation (2).

In Figure 14, we show the azimuthally–averaged radial distribution of the [C ɪɪ] excess emissivity (top panel), of the corresponding C^+ column density (middle panel), and of the CO–dark H_2 column density (lower panel). The steep distribution of the [C ɪɪ] excess emissivity, with a peak at 4.2 kpc, becomes flatter when converted to $N(C^+)$ as a result of applying the $n(H_2)$ gradient derived from Equation (3) and a constant $T^{\rm H_2}_{\rm kin}$ equal to 70 K. When applying the [C]/[H_2] abundance gradient, the radial distribution of CO–dark H_2 becomes nearly constant between 4 and 11 kpc. We will discuss this flat distribution of the CO–dark H_2 column density and relate it to the denser H_2 gas traced by CO and ^{13}CO in Section 5.3. Note that when calculating column densities we are assuming that the [C ɪɪ] emission is extended with respect to the beam of our observations. In the case that there is substructure within the beam, our estimate of the column density will be a lower limit, as it corresponds to that averaged over *Herschel*'s 12″ beam.

In Figure 15 we show the resulting CO–dark H_2 column density distribution for different combinations of the kinetic temperature in the H ɪ and H_2 layers. The volume densities are obtained from Equation (3), considering the factor 1.6 correction for H_2 gas discussed above. We assume that the temperature of the H_2 layer is equal to or lower than the temperature of the H ɪ layer. For each kinetic temperature, the corresponding value of R_{ul} was interpolated from data calculated by Flower & Launay (1977) for collisions with H_2 and by Launay & Roueff (1977) for collisions with H. As we can see, for a wide range of temperature combinations, the derived column density deviates by about 30% from our adopted model with $T^{\rm HI}_{\rm kin}$ = 100 K and $T^{\rm H_2}_{\rm kin}$ = 70 K. We therefore consider that our CO–dark H_2 column density determination has a 30% uncertainty.

5.2.2. H_2 gas traced by ^{12}CO and ^{13}CO

A commonly employed method to estimate the H_2 mass of molecular clouds is the use of the ^{13}CO integrated intensity, $I(^{13}CO)$, to derive the ^{13}CO column density, $N(^{13}CO)$, assuming that this line is optically thin and that local thermodynamic equilibrium (LTE) applies. $N(^{13}CO)$ can be then converted to N(CO), assuming an appropriate isotopic ratio, and N(CO) to $N(H_2)$, assuming a CO abundance relative to H_2. It has been observed in large–scale ^{12}CO and ^{13}CO surveys, however, that the spatial extent of the ^{13}CO emission is often noticeably smaller than, and is contained within, the observed extent of the ^{12}CO emission (Goldsmith et al. 2008; Roman-Duval et al. 2010). This spatial discrepancy is mostly due to the limited sensitivity of the observations that is often inadequate to detect the weak ^{13}CO emission emerging from the envelopes of molecular clouds. The region where only ^{12}CO is detected but ^{13}CO is not can account for ∼30% of the total mass of a molecular cloud (Goldsmith et al. 2008; Pineda et al. 2010a). The discrepancy between the spatial extent of these two lines is also seen in the position velocity maps of the observed ^{12}CO and ^{13}CO lines obtained as part of the GOT C+ survey.

To estimate the azimuthally averaged H_2 column density traced by CO and ^{13}CO for each ring, we considered two cases: spaxels where both ^{12}CO and ^{13}CO are detected (Mask CO2) and spaxels where ^{12}CO is detected but ^{13}CO is not (Mask CO1). In Figure 16, we show the radial distribution of the azimuthally averaged ^{12}CO and ^{13}CO emissivity for spaxels in Masks CO1 and CO2. Although by definition spaxels in Mask CO1 have ^{13}CO intensities below the sensitivity limit, we could nevertheless detect ^{13}CO emission for spaxels in this mask region after averaging them in azimuth as seen in the figure. As ^{13}CO can be considered optically thin, the integrated intensity of this line is proportional to the ^{13}CO column density which in turn should be proportional to the H_2 column density. Thus, spaxels in Masks CO2 and CO1 correspond to regions with larger and smaller column densities, respectively, with the threshold between these two column density regimes given by the sensitivity of the ^{13}CO observations.

In the following we describe our procedure used to estimate H_2 column densities from Mask CO1 and Mask CO2. The procedure is very similar to that used in the Taurus molecular cloud by Pineda et al. (2010a) and Goldsmith et al. (2008). We refer to these papers for further details on the column density determination. We derived the H_2 column density using the ^{12}CO and ^{13}CO emissivities calculated from spaxels where the ^{12}CO and/or ^{13}CO are detected. We later expressed the derived H_2 column density as an average that considers all sampled spaxels within a given Galactocentric ring, not only where ^{12}CO and ^{13}CO emission is detected, to facilitate the comparison with the column density of CO–dark H_2 gas (Section 5.2.1).

For Mask CO2, we estimated $N(^{13}\mathrm{CO})$ from $I(^{13}\mathrm{CO})$ under the assumption that this line is (almost) optically thin and that LTE applies. Apart from the dependence on $I(^{13}\mathrm{CO})$, $N(^{13}\mathrm{CO})$ depends on the excitation temperature, T_{ex}, and opacity corrections that might apply. The excitation temperature and the optical depth can be derived from the peak line intensity of the ^{12}CO and ^{13}CO lines, respectively. To derive the line peak intensities we assumed that the average ^{12}CO or ^{13}CO emissivities are equivalent to the average of the integrated intensity of a number of Gaussian lines with equal FWHM line width of 3 km s^{-1}, which is a typical value for the observed ^{12}CO and ^{13}CO lines in our survey (Langer et al. 2013 in preparation). Note that the calculation of T_{ex} also assumes that the ^{12}CO line is optically thick ($\tau >> 1$). Accounting for opacity in the derivation of $N(^{13}\mathrm{CO})$ typically results in only a 10% correction.

We converted $N(^{13}\mathrm{CO})$ to $N(\mathrm{CO})$ using the slope of the ^{12}C/^{13}C isotope ratio gradient derived by Savage et al. (2002), while fixing the ^{12}C/^{13}C isotope ratio to be 65 at $R_{\mathrm{gal}} = 8.5$ kpc. The ^{12}C/^{13}C isotope ratio as a function of Galactocentric distance is thus given by

$$\frac{^{12}\mathrm{C}}{^{13}\mathrm{C}} = 4.7\left(\frac{R_{\mathrm{gal}}}{\mathrm{kpc}}\right) + 25.05, \tag{4}$$

where R_{gal} is the Galactocentric distance. For this gradient, the isotopic ratio varies from ∼43 to ∼80 for Galactocentric distance between 4 kpc and 12 kpc. We converted $N(\mathrm{CO})$ to $N(\mathrm{H_2})$ using a $[\mathrm{CO}]/[\mathrm{H_2}]$ abundance gradient constructed using the slope of the [C]/[H] abundance gradient in Equation (2) fixing $[\mathrm{CO}]/[\mathrm{H_2}]=1 \times 10^{-4}$ at R_{gal} =8.5 kpc.

As noted by e.g. Tielens (2005), the $[\mathrm{CO}]/[\mathrm{H_2}]$ relative abundance used here, and widely used in the literature, is a factor of 3 lower than the gas-phase carbon abundance observed in the diffuse ISM, used in Section 5.2.1. This reduced CO fractional abundance is inconsistent with chemical models that predict that, in well shielded regions, all the gas–phase carbon should be in the form of CO (Solomon & Klemperer 1972; Herbst & Klemperer 1973). This discrepancy is not a result of CO molecules frozen onto dust grains, as it persist even after a correction to account for CO and CO_2 ices is applied (Whittet et al. 2010; Pineda et al. 2010a). The CO/H_2 abundance is often derived by comparing observations of CO and ^{13}CO with visual extinction maps towards well studied nearby dark clouds (e.g. Dickman 1978; Frerking et al. 1982; Pineda et al. 2010a). When the contribution from H I gas is subtracted, the visual extinction traces the total column of H_2 along the line of sight. However, a certain column of H_2 is required to shield the FUV photons before CO can form. Therefore, for a given path length, only a fraction of it, its central part, will have all gas–phase carbon in the form of CO, while the remainder will be what we call the CO–dark H_2 gas. Dividing the column density of CO with that of H_2 will result in a fractional abundance that is lower than what would result if CO is the dominant form of carbon over the entire path length. This effect is more prominent in regions with moderate column densities, which represent the bulk of the mass in giant molecular clouds, where the CO–dark H_2 and CO–traced layers are comparable. Following this argument, the local values, $[\mathrm{C}]/[\mathrm{H_2}]=2.8 \times 10^{-4}$ and $[\mathrm{CO}]/[\mathrm{H_2}]=1 \times 10^{-4}$, would imply a CO–dark H_2 gas fraction of 0.6, which is consistent with what is shown in Figure 19 and that independently found by Paradis et al. (2012) studying the CO–dark H_2 fraction in the Solar neighborhood using extinction mapping. Note that by using $[\mathrm{CO}]/[\mathrm{H_2}]=1 \times 10^{-4}$ in our calculations we are implicitly accounting for the contribution from CO–dark H_2 gas in the derivation of the H_2 column density from CO and ^{13}CO. The CO–dark H_2 gas present in regions traced by CO and ^{13}CO will be studied in detail by Langer et al. (2013 in preparation).

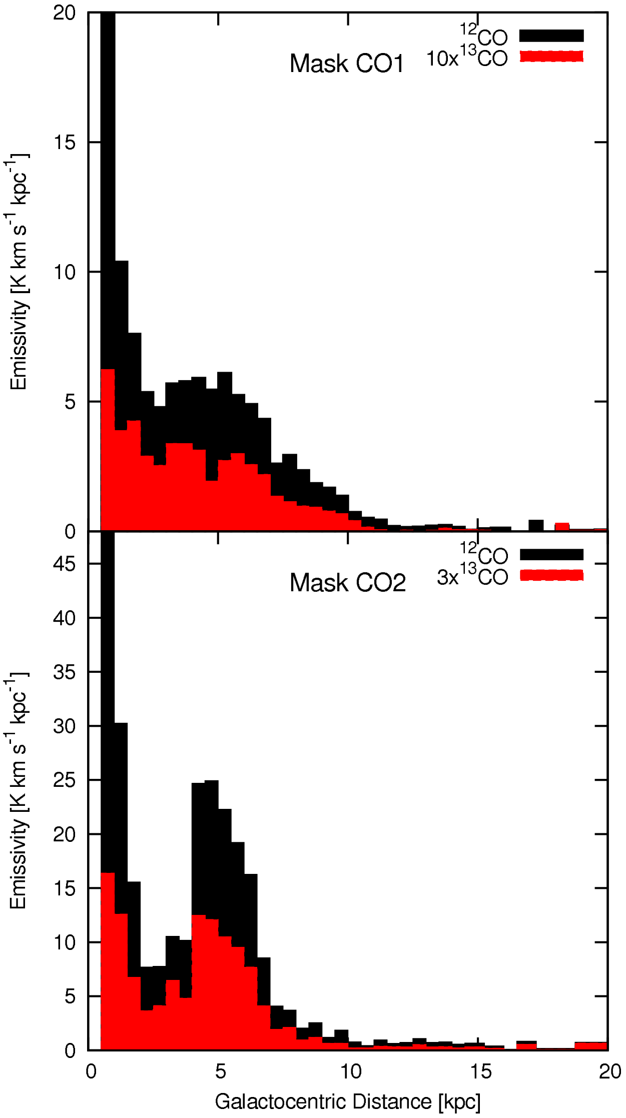

Fig. 16. Radial distribution of the azimuthally averaged ^{12}CO and ^{13}CO emissivities observed in the Galactic plane for the case where ^{12}CO is detected in individual spaxels but ^{13}CO is not (Mask CO1; upper panel), and for the case where both ^{12}CO and ^{13}CO are detected in individual spaxels (Mask CO2; lower panel). Typical uncertainties of the ^{12}CO and ^{13}CO emissivities are 0.1 and 0.02 K km s^{-1} kpc^{-1}, respectively.

As noted above, spaxels in Mask CO1 correspond to low H_2 column density gas. For molecular clouds it is likely that this gas is also characterized by low H_2 volume densities. Assuming that the detected ^{12}CO emission in Mask CO1 is nonetheless optically thick we estimated the excitation temperature as we did for Mask CO2. Typical values were found to be in the 4 K to

6 K range for 4 kpc $\leq R_{\rm gal} \leq$ 12 kpc. As seen in Taurus, pixels in Mask CO1 are located in the periphery of the large column density molecular cloud traced by ^{12}CO and ^{13}CO (Mask CO2). However, the excitation temperatures estimated for Mask CO1 are lower than those derived for Mask CO2 (∼10–20 K), and therefore they are inconsistent with what we would expect for this gas being in LTE, because the kinetic temperature is likely to be higher in the outer regions of the cloud which are subject to increased heating. It is therefore reasonable to assume that the gas in Mask CO1 is subthermally excited. Pineda et al. (2010a) used the RADEX (van der Tak et al. 2007) excitation/radiative transfer code to predict line intensities from a gas with conditions similar to those of Mask CO1 in the envelope of the Taurus molecular cloud. RADEX accounts for effects of trapping, which are important for the excitation of CO at low densities. The model parameters are the kinetic temperature, $T_{\rm kin}$, the H_2 volume density, $n(H_2)$, the CO column density per unit line width, $N({\rm CO})/\delta v$, and the ^{12}CO/^{13}CO abundance ratio, R. The observed parameters are the excitation temperature and the ^{12}CO/^{13}CO integrated intensity ratio. As mentioned above, the excitation temperature varies from 6 K to 4 K for 4 kpc $\leq R_{\rm gal} \leq$ 12 kpc. The ^{12}CO/^{13}CO integrated intensity ratio shows little variation from its average value of ∼24 for the same range in Galactocentric distance. We assume that the kinetic temperature is 15 K. If the value of R were known, one could find a unique solution for $n(H_2)$ and N(CO). However, the isotopic ratio is expected to vary from that expected for well–shielded regions due to isotopic enhancements produced by chemical and/or photo effects. Thus, there is a family of solutions that can reproduce the observed quantities. Pineda et al. (2010a) used nearly 10^6 individual spectra in the Taurus molecular cloud to find a set of solutions that produced a monotonically decreasing R with decreasing excitation temperature and a smoothly decreasing column density with decreasing excitation temperature. The observed ^{12}CO/^{13}CO integrated intensity ratio for a given value of $T_{\rm ex}$ for all Galactocentric rings is in excellent agreement with the same quantities observed in the envelope of the Taurus molecular cloud. We therefore used the solution presented in Pineda et al. (2010a) to derive the N(CO) column density in Mask CO1 for each Galactocentric ring. For our observed values of $T_{\rm ex}$ and the ^{12}CO/^{13}CO integrated intensity ratio, their solution suggests a gas with $n(H_2) \simeq 250\,{\rm cm}^{-3}$ and $R \simeq 30$. We use their fit to the relationship between CO column density and the observed excitation temperature given by

$$\left(\frac{N({\rm CO})}{\rm cm^{-2}}\right)\left(\frac{\delta v}{\rm km\,s^{-1}}\right)^{-1} = 6.5\times10^{13}\left(\frac{T_{\rm ex}}{\rm K}\right)^{2.7} \qquad (5)$$

to derive the average N(CO) column density in Mask CO1.

The [CO]/[H_2] abundance ratio is expected to show strong differences between UV–exposed and shielded regions as a result of the competition between the formation and destruction of CO (e.g. van Dishoeck & Black 1988; Visser et al. 2009). Pineda et al. (2010a) compared CO column densities derived at the envelope of the Taurus molecular cloud with a visual extinction, $A_{\rm V}$, map of the same region (with the contribution from dust associated with atomic gas to the visual extinction subtracted). They provided a polynomial fit giving $A_{\rm V}$ at any given value of N(CO) (see their Figures 13 and 14). We use this fit to derive visual extinctions from N(CO) in Mask CO1. Since $A_{\rm V}$ traces the total column density of H_2, not only that traced by CO, the relationship between N(CO) and $A_{\rm V}$ should already account for the CO–dark H_2 gas present in the envelope of the Taurus molecular cloud. The visual extinction outside the CO boundary in Taurus can be estimated by searching for the value of $A_{\rm V}$ at which $N({\rm CO}) = 0\,{\rm cm}^{-2}$. A polynomial fit to the lower part of the N(CO)–$A_{\rm V}$ relationship gives $N({\rm CO}) = 0\,{\rm cm}^{-2}$ for $A_{\rm V}$=0.37 mag. Note that this correction only applies if the column density in Mask CO1 is derived using spaxels that have both [C II] and ^{12}CO emission. There are, however, spaxels in Mask CO1 where ^{12}CO emission is detected but [C II] is not, and the correction in the conversion from N(CO) to $A_{\rm V}$ does not apply to them, because their CO–dark H_2 layer is not already traced by [C II]. We repeated the column density estimation described above but for only spaxels in Mask CO1 that have both [C II] and ^{12}CO emission as well as for those that have ^{12}CO emission but no [C II]. After applying the 0.37 mag correction to the column density distribution derived from spaxels detected in [C II] and ^{12}CO and adding it to that derived from spaxels with ^{12}CO emission only, we find that the total column density distribution is about 15% lower than that without applying the correction. We therefore reduce the derived values of $A_{\rm V}$ by 15% to account for the CO–dark H_2 gas already traced by [C II] in Mask CO1.

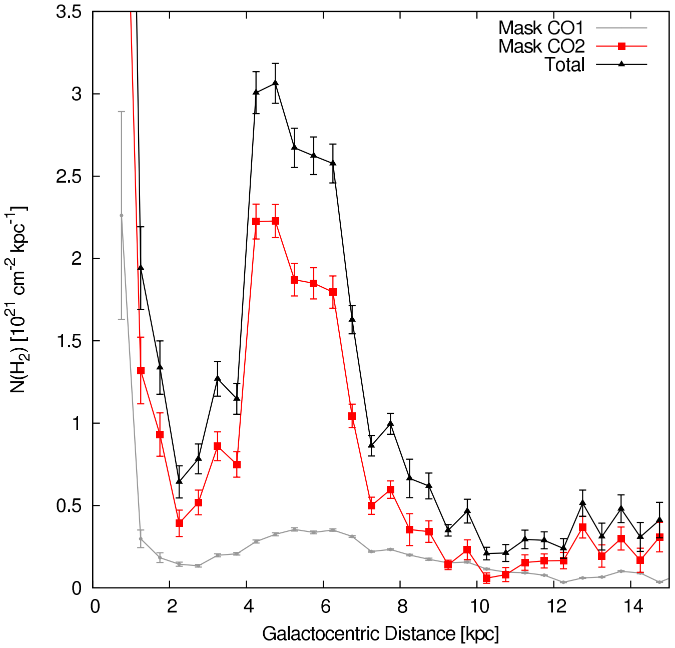

Fig. 17. Radial distribution of the azimuthally averaged H_2 column density as traced by ^{12}CO and ^{13}CO. We include the radial distribution of $N(H_2)$ from gas associated with spaxels where both ^{12}CO and ^{13}CO are detected (Mask CO2) and where ^{12}CO is detected but ^{13}CO is not (Mask CO1). The total distribution (Mask CO1+ Mask CO2) has been increased by 20% to account for ^{12}CO emission that is not detected in individual spaxels but was detected after averaging them in azimuth (see Section 5.2.2).

The formation of CO in cloud envelopes is mostly influenced by dust grains shielding the FUV radiation field, with smaller contributions from H_2 shielding and CO self–shielding. Thus, changes in metallicity will not significantly influence the dust column density, but will modify the H_2 column density, at which the C$^+$/C^0/CO transition takes place, because a reduction/increase on metallicity is associated with a increase/reduction of the gas–to–dust ratio, $R_{\rm gd} = N(H_2)/A_{\rm V}$. To convert the derived visual extinctions to H_2 column densities, we assumed that $R_{\rm gd}$ has the same slope, but with the opposite sign, of the galactic metallicity gradient (Equation 2), and we fixed its value at $R_{\rm gal}$ = 8.5 kpc to be $9.4\times10^{20}{\rm cm}^{-2}\,{\rm mag}^{-1}$ (Bohlin et al.

1978). The resulting gas to dust ratio as a function of galactocentric distance is therefore given by,

$$R_{\rm gd} = 2.38\times10^{20}10^{0.07R_{\rm gal}}\ {\rm cm^{-2}/mag}, \quad (6)$$

with the galactocentric distance, $R_{\rm gal}$, in units of kpc. We applied this relationship to convert from $A_{\rm V}$ to $N({\rm H_2})$ in Mask CO1.

Pineda et al. (2010a) and Goldsmith et al. (2008) detected ^{12}CO and ^{13}CO emission in the periphery of Taurus where these lines were not detected in individual pixels. Pineda et al. (2010a) estimated that this gas accounts for about 20% of the total mass of Taurus. Although we can still detect weak ^{12}CO emission after averaging in azimuth regions where ^{12}CO is not detected in individual spaxels, we could not detect ^{13}CO, and therefore cannot repeat the analysis done in Taurus. We corrected the total column density traced by ^{12}CO and ^{13}CO by 20% to account for this missing CO gas component.

Figure 17 shows the total azimuthally averaged H_2 column density as traced by ^{12}CO and ^{13}CO. For the range between 4 kpc and 7 kpc, gas associated with Mask CO2 contributes about 70% of the total H_2 traced by CO and ^{13}CO. For 7 kpc< $R_{\rm gal}$ <10 kpc, the gas associated with Mask CO2 contributes about 25% of the total CO–traced H_2 gas. This contribution is consistent with the relative contribution from Mask CO1 and Mask CO2 to the mass of the nearby Taurus molecular cloud derived by Pineda et al. (2010a).

5.3. The complete distribution of H_2 in the plane of the Milky Way

In Figure 18, we show the radial distribution of the total azimuthally averaged H_2 column density. The total $N(H_2)$ is the combination of the contribution from H_2 gas traced by CO and that traced by [C II] (CO–dark H_2 gas). Both contributions are also included in the figure. Close to the Galactic center, most of the H_2 is traced by CO with the CO–dark H_2 gas making a negligible contribution. The CO–traced H_2 gas is mostly concentrated in the 4 kpc to 7 kpc range, while the CO–dark H_2 gas is extended over a wider range of Galactocentric distances, between 4 and 11 kpc. As mentioned in Section 5.2.1, the distribution of the CO–dark H_2 column density is nearly constant between 4 and 11 kpc. However, the fraction of the total molecular gas in this component increases with Galactocentric distance. This increase is shown in Figure 19 where we show the CO–dark H_2 gas fraction as a function of Galactocentric distance. The fraction of CO–dark H_2 gas increases monotonically with Galactocentric distance, rising from 0.2 of the total H_2 gas at 4 kpc to be about 0.8 at 10 kpc. The Galactic metallicity gradient is likely accompanied by a decrease of the dust–to–gas ratio with Galactocentric distance. The reduced dust extinction results in an increased FUV penetration, which in turn results in the C^+/C^0/CO transition layer taking place at larger H_2 column densities. Thus, as suggested by our results, the low–column density H_2 gas at large Galactocentric distances, with low–metallicities, is better traced by [C II] (and perhaps [C I]) than by CO.

For $R_{\rm gal}$ > 11 kpc, we see a reduction of the column density of CO–dark H_2 gas. In the outer Galaxy we detect fewer [C II] clouds per unit area and, as we can see in Figure 11, most of the detected emission is associated with dense PDRs. Because of the reduced carbon abundance in the outer Galaxy, and perhaps reduced thermal pressures, the [C II] intensity associated with CO–dark H_2, as well as that associated with H I and electron gas, might be reduced to be below our detection threshold, while only regions associated with star–formation, dense PDRs, can produce detectable emission. Due to the reduced star formation activity per unit area in the outer Galaxy, the average strength of the FUV field is likely also reduced. This reduction of the FUV field results in a lower kinetic temperature that reduce the excitation of [C II] line. Additionally, the plane of the Milky Way is known to warp towards the outer Galaxy, while the CO–dark H_2 distribution is based on [C II] data at b=0°. Thus, our sampling of the outer Galactic plane might not be as good as it is for the inner Galaxy. Therefore we cannot rule out that the distribution of H_2 extends even further in the outer Galaxy than indicated here.

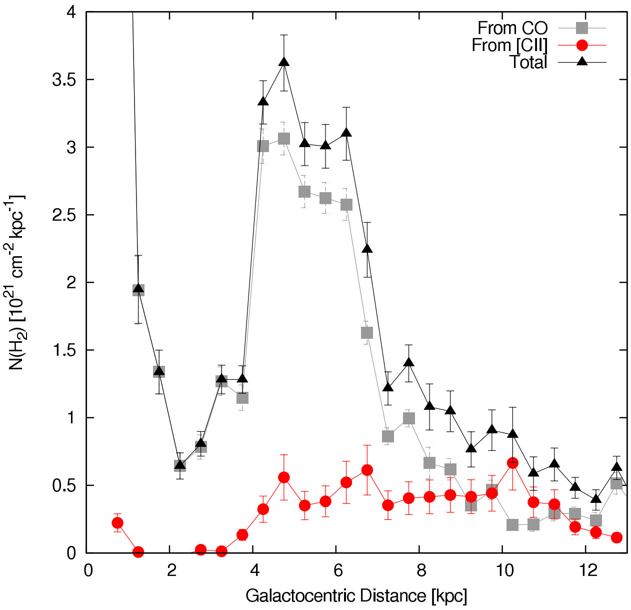

Fig. 18. Radial distribution of the H_2 column density in the plane of the Milky Way. We also show the relative contributions to the total H_2 column density from gas traced by ^{12}CO and ^{13}CO and from CO–dark H_2 gas.

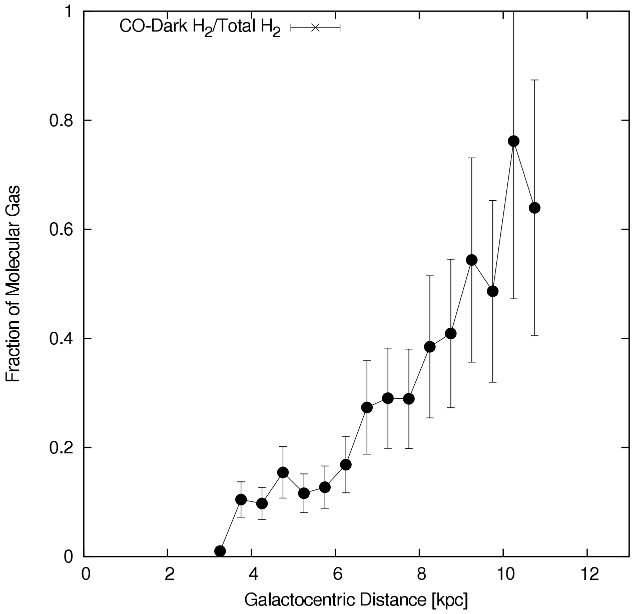

Fig. 19. Radial distribution of the fraction of the total H_2 column density comprised by the CO–dark H_2 gas.

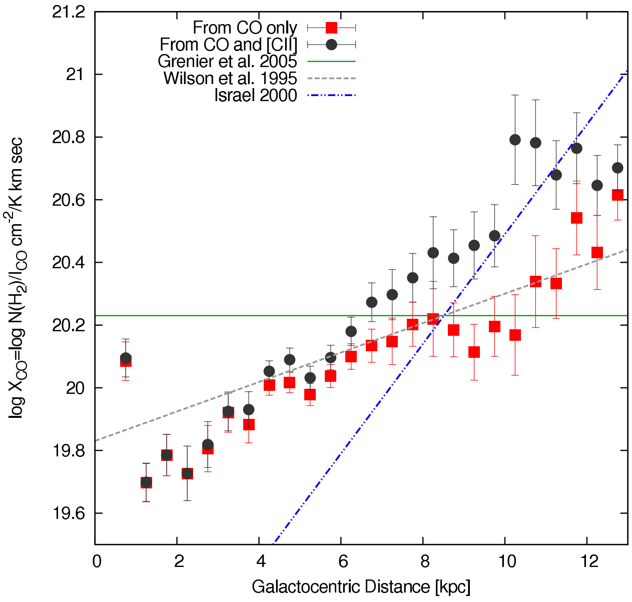

Fig. 20. Radial distribution of the CO–to–H_2 conversion factor. We show the distribution for values estimated considering the CO–traced H_2 gas as well as that including the CO–dark H_2 gas component.

5.4. The CO–to–H_2 conversion factor in the Milky Way

When ^{13}CO observations are not available, the mass of molecular clouds or the molecular content of entire galaxies is often estimated from observations of the ^{12}CO $J = 1 \rightarrow 0$ line applying an empirically–derived CO–to–H_2 conversion factor ($X_{\rm CO} \equiv N({\rm H_2})/I_{\rm CO} \propto M_{\rm H_2}/L_{\rm CO}$). Modelling applied to γ–ray observations, which trace the total molecular content along the line–of–sight, results in a local value of 1.74×10^{20} cm^{-2} (K km s^{-1})$^{-1}$ or $M_{\rm H_2}/L_{\rm CO} = 3.7\,M_\odot$(K Km s^{-1} pc^2)$^{-1}$ (Grenier et al. 2005). Several theoretical studies have focused on the dependence of $X_{\rm CO}$ on environmental conditions, showing that $X_{\rm CO}$ is particularly sensitive to metallicity and the strength of the FUV radiation field (e.g. Maloney & Black 1988; Sakamoto 1996). Observationally, however, it has been found that $X_{\rm CO}$ is mostly sensitive to metallicity (e.g. Rubio et al. 1991; Wilson 1995; Israel 1997, 2000) while not showing a significant dependence on the strength of the FUV field (Pineda et al. 2009; Hughes et al. 2010).

We estimated the radial distribution of $X_{\rm CO}$ in the Galactic plane by dividing the H_2 column density in a given Galactocentric ring by its corresponding ^{12}CO emissivity. In Figure 20 we show the radial distribution of $X_{\rm CO}$ derived from the H_2 column density traced by CO and ^{13}CO only, as well as that including the CO–dark H_2 component. We also show the radial distribution of $X_{\rm CO}$ derived from the relationship between $X_{\rm CO}$ and metallicity observed by Wilson (1995) and Israel (2000) in nearby galaxies. We converted the dependence of $X_{\rm CO}$ on metallicity presented by these authors to a radial dependence using the slope of the metallicity gradient in Equation (2), fixing $X_{\rm CO}$ to be 1.74×10^{20} cm^{-2} (K km s^{-1})$^{-1}$ at $R_{\rm gal} = 8.5$ kpc.

Both $X_{\rm CO}$ distributions increase with the Galactocentric distance. But when the contribution from CO–dark H_2 is included, the slope is steeper. This steeper slope is a result of the monotonic increase of the CO–dark H_2 contribution to the total H_2 column density with Galactocentric distance (Figure 19). The radial distribution of $X_{\rm CO}$ considering $N({\rm H_2})$ from ^{12}CO and ^{13}CO only is consistent with that fitted by Wilson (1995). When CO–dark H_2 is included in the calculation of $X_{\rm CO}$ the radial distribution starts to resemble that fitted by Israel (2000). The offsets of course will change if the normalization at $R_{\rm gal}$=8.5 kpc is adjusted. Note that there is a difference in the method used by Wilson (1995) and Israel (2000) to derive $X_{\rm CO}$. Wilson (1995) observed ^{12}CO in several giant molecular clouds within several nearby galaxies and compared their virial masses to the mass derived from their ^{12}CO luminosities using a Galactic conversion factor. Israel (2000) estimated the H_2 mass of a sample of nearby galaxies by modelling their FIR continuum emission to derive their masses and related them to their ^{12}CO luminosities to derive $X_{\rm CO}$. The FIR continuum emission should trace the total H_2 content (including the CO–dark H_2 component) while the method based on the virial mass derived from ^{12}CO mapping accounts for only the H_2 mass traced by ^{12}CO.

The increase of $X_{\rm CO}$ with Galactocentric distance for the case when only CO and ^{13}CO are used to derive $N({\rm H_2})$ is a result of the abundance gradient we applied in the calculation of $N({\rm H_2})$. If we set the [CO]/[H_2] abundance to be constant when converting N(CO) to $N({\rm H_2})$ for Mask CO2, and from $A_{\rm V}$ to $N({\rm H_2})$ for Mask CO1, we obtain a nearly constant radial distribution of $X_{\rm CO}$. When the CO–dark H_2 is included, however, the slope (seen in Figure 20) results from both the abundance and the thermal pressure gradients. If we also set the [C$^+$]/[H_2] abundance to be constant we still obtain a distribution that increases with $R_{\rm gal}$. Thus, the difference in the slopes in the distribution of $X_{\rm CO}$ is a result of the use of the thermal pressure gradient in the calculation of the CO–dark H_2 column density distribution.

5.5. The surface density distribution and mass of the atomic and molecular gas in the Galactic plane

In the top panel of Figure 21, we show the vertical surface density distribution of the total hydrogen gas in the Galactic plane. We also show the relative contributions from atomic and molecular gas. We calculated the surface densities assuming a Gaussian vertical distribution of the gas. For the molecular gas we assume a constant FWHM disk thickness of 130 pc (Section 3.2). In the case of the atomic gas, the disk thickness is observed to increase with Galactocentric distance, and we used the exponential relation presented by Kalberla & Kerp (2009), $z_{\rm FWHM} = 0.3e^{(R_{\rm gal}-8.5)/9.8}$ kpc. In all cases, the surface density includes a correction to account for the contribution from He. In the lower panel of Figure 21, we show the surface density distribution of the different contributing ISM components of the atomic and molecular gas studied here, the cold and warm neutral medium, the CO–dark H_2 gas, and the H_2 gas traced by ^{12}CO and ^{13}CO. The surface density distribution of atomic and molecular gas derived in our analysis is similar to that derived by Scoville & Sanders (1987), but with the addition of the CO–dark H_2 component, the distribution of molecular gas extends over a larger range of Galactocentric distances compared with that traced by ^{12}CO and ^{13}CO only. In Table 2, we list the mass of each ISM component studied here. The CO–dark H_2 gas accounts for about 30% of the total molecular gas mass. The WNM dominates the mass of atomic gas in the Galactic plane, accounting for 70% of the total atomic mass.

6. The FUV radiation field distribution in the Milky Way

An important parameter governing the thermal balance and chemistry in interstellar clouds is the strength of the FUV field,

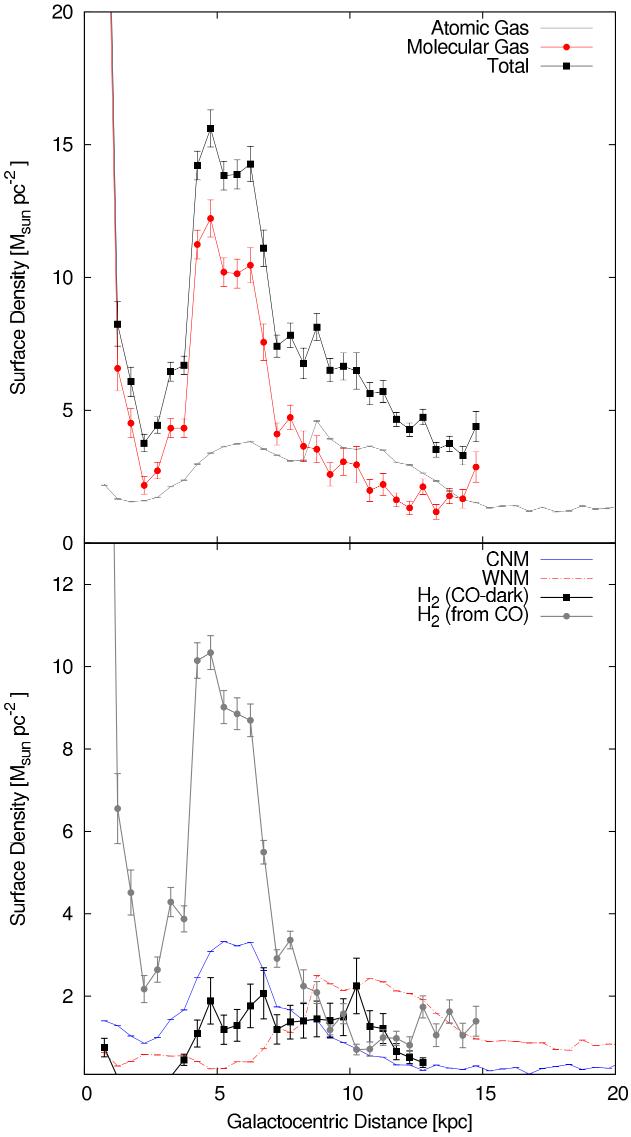

Fig. 21. (*top panel*) Radial distribution of the surface density of hydrogen in the Galactic plane. We also show the contribution of the atomic and molecular hydrogen gas. (*lower panel*) Radial distribution of the different ISM components, including the cold and warm neutral medium (atomic gas), the CO–dark H$_2$ component, and the H$_2$ gas that is traced by ^{12}CO and ^{13}CO. All surface densities have been corrected to account for the contribution of He.

Table 2. Mass of Milky Way ISM components

Component	Mass 10^9 M$_\odot$
H$_2$ from CO	1.9
H$_2$ CO–dark	0.7
H$_2$ Total	2.6
H I CNM	0.9
H I WNM	1.6
H I Total	2.5
Total H I+H$_2$	5.1

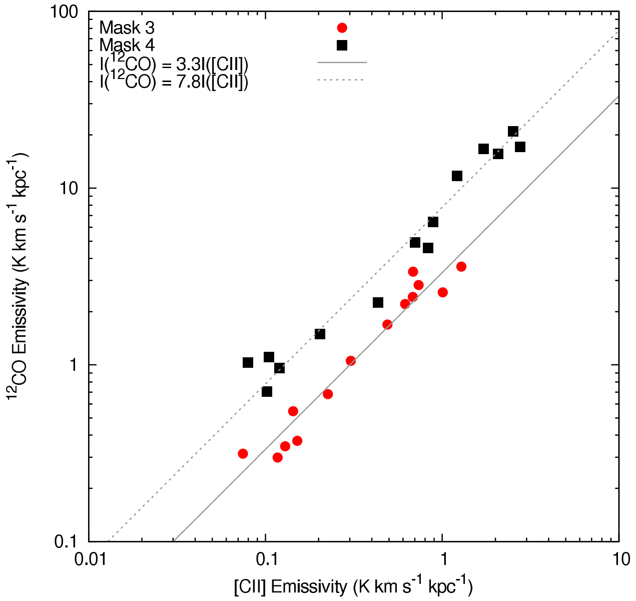

Fig. 22. Comparison between the [C II] and ^{12}CO emissivities corresponding to different Galactocentric rings, for gas associated with Mask 3 (red circles) and Mask 4 (black boxes). The straight lines represent fits to the data. Typical uncertainties are 0.02 and 0.1 K km s^{-1} kpc^{-1}, for [C II] and ^{12}CO, respectively.

χ_0 (in units of the Draine 1978 field). The gas heating in cold, diffuse regions is dominated by the photoelectric effect resulting from the absorption of FUV photons by dust grains and PAHs. The FUV field also plays a critical role in the formation and destruction of CO, determining the column density at which the C$^+$/C^0/CO transition takes place. It is therefore of interest to determine the typical strength of the FUV field to which the interstellar gas is exposed and how this FUV field varies from place to place in the plane of the Milky Way.

PDR model calculations suggest that the [C II]/^{12}CO integrated intensity ratio is primarily a function of χ_0 and the total H ($n_{\rm HI} + 2n_{\rm H_2}$) volume density (Wolfire et al. 1989; Kaufman et al. 1999). The reason for this dependence is that the ^{12}CO emission becomes optically thick quickly after a modest fraction of the gas–phase carbon is converted to CO. The [C II]/^{12}CO ratio is thus determined by the column density of C$^+$ and the temperature of the line–emitting region. Both quantities depend, in turn, on the strength of FUV field and H volume density. The solution for a given value of the [C II]/^{12}CO ratio is not unique, however, and several pairs of χ_0 and $n_{\rm H}$ can reproduce the observations. Therefore, we can only use the [C II]/^{12}CO ratio to determine a range of plausible values of the FUV radiation field and H volume density that characterize the line–emitting region.

In a preliminary study of [C II], ^{12}CO, and ^{13}CO velocity components on 16 GOT C+ LOSs, Pineda et al. (2010b) used PDR model calculations to constrain the strength of the FUV field to be mostly χ_0 =1–10, over a wide range of H$_2$ volume densities, thus suggesting that most of the observed [C II] emission associated with ^{12}CO and ^{13}CO is exposed to weak FUV radiation fields. A similar result, was obtained from PDR modeling of the [C II] emission observed by COBE by Cubick et al. (2008), suggesting that most of the [C II] in our Galaxy originates in a clumpy medium exposed to an FUV field of $\chi_0 \simeq 60$.

With the complete GOT C+ survey, we can study the [C II]/^{12}CO ratio over the entire Galactic plane and determine how the strength of the FUV field is distributed in the Galaxy. We consider the azimuthally averaged emissivity of [C II] calculated from spaxels where both ^{12}CO and ^{13}CO emission is detected (Mask 4), and where ^{12}CO is detected but ^{13}CO is not

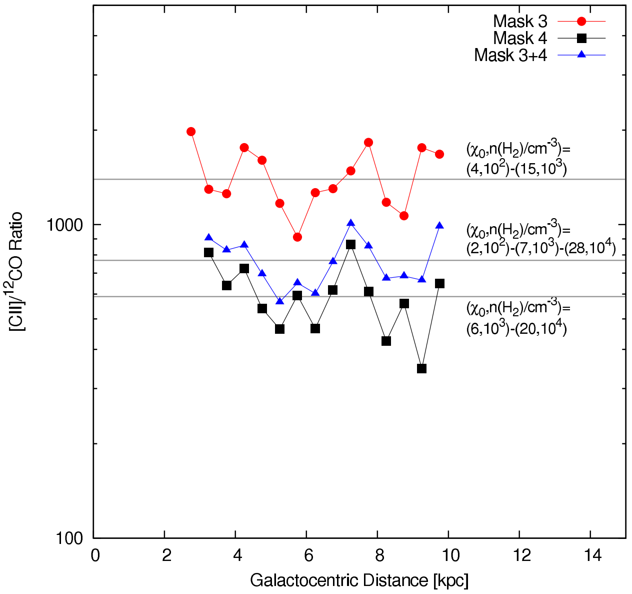

Fig. 23. Radial distribution of the [C II] to ^{12}CO emissivity ratio for Mask 3 (red circles) and Mask 4 (black boxes). We also show the radial distribution of the [C II]/^{12}CO ratio resulting from the combined emission from Mask 3 and 4 (blue triangles). The horizontal lines correspond to the average value for each Mask region between 3–10 kpc. The horizontal lines are labeled with a range of pairs of the FUV field and H_2 volume densities (χ_0, n_{H_2}), that reproduce their corresponding [C II]/^{12}CO ratio, as predicted by the Kaufman et al. (1999) PDR model. To facilitate the comparison with the PDR model, the ratios were calculated using [C II] and ^{12}CO emissivities expressed in units of erg s^{-1} cm^{-2} sr^{-1} kpc^{-1}. In these units, typical uncertainties in the ratios are 180, 33, and 35 for Mask 3, Mask 4, and the combined emission from both Mask regions, respectively.

(Mask 3; See Figure 9). As discussed in Section 4, gas associated with Mask 3 might represent low–column density gas surrounding the high–column density regions associated with Mask 4. In Figure 22, we show a comparison between the [C II] and ^{12}CO intensities for different Galactocentric rings, for gas associated with Mask 3 and 4. In both mask regions we see a good correlation between these two emissivities. A straight line fit results in $I(^{12}\mathrm{CO}) = 7.8I([\mathrm{C\,II}])$, for Mask 3, and $I(^{12}\mathrm{CO}) = 3.3I([\mathrm{C\,II}])$ for Mask 4.

In Figure 23, we show the radial distribution of the [C II] to ^{12}CO emissivity ratio for Masks 3 and 4. We also include the radial distribution of the [C II]/^{12}CO ratio resulting from the combined emission from Masks 3 and 4. The ratio is computed considering emissivities in units of erg s^{-1} cm^{-2} sr^{-1} kpc^{-1}. We restrict the range in Galactocentric distance to be between 3 and 10 kpc because, for these regions, both [C II] and ^{12}CO have significant emission in this range. As expected, given the linear correlation between [C II] and ^{12}CO, the ratio shows little variation between 3 and 10 kpc. We also include horizontal lines representing the average [C II]/^{12}CO ratio for each mask region. These horizontal lines are labeled with a range of pairs of the FUV field and H_2 volume densities (χ_0, n_{H_2}), that can reproduce the corresponding values of the [C II]/^{12}CO ratio, as predicted by the PDR model calculations from Kaufman et al. (1999). As mentioned before, Mask 3 might represent regions with lower column densities compared to those in Mask 4. This column density difference might also translate into a difference in volume densities because we do not expect a large difference in the spatial extent of such regions. We thus show the results of the PDR model for ranges in n_{H_2} that, based on the analysis in Section 5.2.2, might be appropriate. We considered the range of H_2 volume density 10^2–10^3 cm^{-3} for Mask 3, and 10^3–10^4 cm^{-3} for Mask 4. For the combined emission from Mask 3 and Mask 4, we considered a wider range of possible H_2 volume densities 10^2 – 10^4 cm^{-3}. Note that the PDR model calculations presented by Kaufman et al. (1999) are in terms of the total H volume density, including atomic and molecular hydrogen. For the comparison between the observations and model predictions we assumed that the contribution of atomic hydrogen to the total H volume density is negligible and show the results of the PDR model in terms of the H_2 volume density.

We find that over the selected range of H_2 volume densities, the [C II]/^{12}CO ratio in both Mask 3 and Mask 4 suggest values of χ_0 that are in the range 1–30, while we do not find any systematic variation in χ_0 with Galactocentric distance between 3 kpc and 10 kpc. The same range of χ_0 is suggested by the [C II]/^{12}CO ratio resulting from the combined emission from Mask 3 and 4, over a wider range of H_2 volume densities. Our results therefore suggest that on average the [C II] emission associated with ^{12}CO and/or ^{13}CO observed in the Galactic plane by the GOT C+ survey emerges from gas exposed to modest FUV radiation fields, away from massive star–forming regions.

7. Summary

In this paper we have presented results of our study of the distribution and properties of the different ISM components in the plane of the Milky Way using spatially and velocity resolved observations of the [C II] 158μm line. Our results can be summarized as follows:

1. We presented the first longitude–velocity maps of the [C II] 158μm line in the plane of the Milky Way. We found that the [C II] emission is mostly associated with the spiral arms, tracing the envelopes of evolved clouds as well as clouds that are in the transition between the atomic and molecular phases.
2. We found that most of the [C II] emission in the Galactic plane emerges from Galactocentric distances between 4 kpc and 11 kpc.
3. We estimated that most of the observed [C II] emission emerges from dense photon dominated regions (~47%), with smaller contributions from CO–dark H_2 gas (~28%), cold atomic gas (~21%), and ionized gas (~4%).
4. We used the [C II] emission to separate the WNM and CNM contributions in the Galactic plane. We find that most of the atomic gas inside the Solar radius is in the form of cold neutral medium, while the warm neutral medium gas dominates the outer Galaxy. The average fraction of the total atomic gas that is CNM is ~43%.
5. We found that the warm and diffuse CO–dark H_2 is distributed over a larger range of Galactocentric distances (4–11 kpc) than the cold and dense H_2 gas traced by ^{12}CO and ^{13}CO (4–8 kpc). The fraction of the total H_2 gas that is CO-dark H_2 increases with Galactocentric distance, ranging from ~20% at 4 kpc up to ~80% at 10 kpc. We estimate that the CO–dark H_2 gas component accounts for ~30% of the total molecular gas mass in the Milky Way.
6. We estimated the radial distribution of the CO–to–H_2 conversion factor. When $N(H_2)$ is derived from ^{12}CO and ^{13}CO only, the CO–to–H_2 conversion factor increases with

Galactocentric distance, influenced by the Galactic metallicity gradient. When the contribution of CO–dark H_2 gas is included in $N(H_2)$, the CO–to–H_2 conversion factor increases with Galactocentric distance with an steeper slope, which is influenced by both metallicity and thermal pressure gradients.

7. We estimated the average strength of the FUV field modelling the [C ii]/^{12}CO ratio. We find that most of the observed [C ii] emission emerging from dense PDRs is associated with modest FUV fields in the $\chi_0 \simeq 1 - 30$ range.

Our results confirm that [C ii] is an important tool to characterize the different components of the ISM. Large–scale mapping of the Milky Way and nearby galaxies with orbital and sub–orbital observatories are essential to further characterize the lifecycle of the interstellar medium, and will help us to build important templates for the interpretation of observations of [C ii] at high–redshift.

Acknowledgements. This research was conducted at the Jet Propulsion Laboratory, California Institute of Technology under contract with the National Aeronautics and Space Administration. We thank the staffs of the ESA and NASA Herschel Science Centers for their help. We would like to thank Roberto Assef for enlightening discussions. The Galactic Arecibo L-Band Feed Array H i (GALFA–H i) Survey data set was obtained with the Arecibo L-band Feed Array (ALFA) on the Arecibo 305m telescope. Arecibo Observatory is part of the National Astronomy and Ionosphere Center, formerly operated by Cornell University under Cooperative Agreement with the National Science Foundation of the United States of America. © 2013 California Institute of Technology. Government sponsorship acknowledged.

References

Bennett, C. L., Fixsen, D. J., Hinshaw, G., et al. 1994, ApJ, 434, 587
Bohlin, R. C., Savage, B. D., & Drake, J. F. 1978, ApJ, 224, 132
Boreiko, R. T. & Betz, A. L. 1991, ApJ, 380, L27
Boreiko, R. T., Betz, A. L., & Zmuidzinas, J. 1988, ApJ, 325, L47
Cardelli, J. A., Meyer, D. M., Jura, M., & Savage, B. D. 1996, ApJ, 467, 334
Carey, S. J., Noriega-Crespo, A., Mizuno, D. R., et al. 2009, PASP, 121, 76
Cordes, J. M. & Lazio, T. J. W. 2002, ArXiv Astrophysics e-prints
Cubick, M., Stutzki, J., Ossenkopf, V., Kramer, C., & Röllig, M. 2008, A&A, 488, 623
Dame, T. M., Hartmann, D., & Thaddeus, P. 2001, ApJ, 547, 792
de Graauw, T., Helmich, F. P., Phillips, T. G., et al. 2010, A&A, 518, L6+
Dickey, J. M. & Lockman, F. J. 1990, ARA&A, 28, 215
Dickey, J. M., Salpeter, E. E., & Terzian, Y. 1977, ApJ, 211, L77
Dickey, J. M., Strasser, S., Gaensler, B. M., et al. 2009, ApJ, 693, 1250
Dickman, R. L. 1978, ApJS, 37, 407
Draine, B. T. 1978, ApJS, 36, 595
Field, G. B., Goldsmith, D. W., & Habing, H. J. 1969, ApJ, 155, L149
Flower, D. R. & Launay, J. M. 1977, Journal of Physics B Atomic Molecular Physics, 10, 3673
Frerking, M. A., Langer, W. D., & Wilson, R. W. 1982, ApJ, 262, 590
Goldsmith, P. F., Heyer, M., Narayanan, G., et al. 2008, ApJ, 680, 428
Goldsmith, P. F., Langer, W. D., Pineda, J. L., & Velusamy, T. 2012, ApJS, 203, 13
Graf, U. U., Simon, R., Stutzki, J., et al. 2012, A&A, 542, L16
Grenier, I. A., Casandjian, J.-M., & Terrier, R. 2005, Science, 307, 1292
Haffner, L. M., Dettmar, R.-J., Beckman, J. E., et al. 2009, Reviews of Modern Physics, 81, 969
Heiles, C. 1994, ApJ, 436, 720
Heiles, C. & Troland, T. H. 2003, ApJ, 586, 1067
Herbst, E. & Klemperer, W. 1973, ApJ, 185, 505
Heyer, M. H., Brunt, C., Snell, R. L., et al. 1998, ApJS, 115, 241
Higgins, D. R. 2011, PhD thesis, National University of Ireland Maynooth
Higgins, R. D. & Kooi, J. W. 2009, in Society of Photo-Optical Instrumentation Engineers (SPIE) Conference Series, Vol. 7215, Society of Photo-Optical Instrumentation Engineers (SPIE) Conference Series
Hollenbach, D. J. & Tielens, A. G. G. M. 1999, Reviews of Modern Physics, 71, 173
Hughes, A., Wong, T., Ott, J., et al. 2010, MNRAS, 406, 2065
Israel, F. 2000, in Molecular hydrogen in space, Cambridge, UK: Cambridge University Press, 2001. xix, 326 p.. Cambridge contemporary astrophysics. Edited by F. Combes, and G. Pineau des Forêts. ISBN 0521782244, p.293, ed. F. Combes & G. Pineau Des Forets, 293
Israel, F. P. 1997, A&A, 328, 471
Kalberla, P. M. W. & Kerp, J. 2009, ARA&A, 47, 27
Kaufman, M. J., Wolfire, M. G., Hollenbach, D. J., & Luhman, M. L. 1999, ApJ, 527, 795
Kolpak, M. A., Jackson, J. M., Bania, T. M., & Dickey, J. M. 2002, ApJ, 578, 868
Kulkarni, S. R. & Heiles, C. 1987, in Astrophysics and Space Science Library, Vol. 134, Interstellar Processes, ed. D. J. Hollenbach & H. A. Thronson, Jr., 87–122
Ladd, N., Purcell, C., Wong, T., & Robertson, S. 2005, PASA, 22, 62
Langer, W. D., Velusamy, T., Pineda, J. L., et al. 2011, in MW2011 The Milky Way In The Herschel Era:, http://mw2011.ifsi-roma.inaf.it/
Langer, W. D., Velusamy, T., Pineda, J. L., et al. 2010, A&A, 521, L17
Launay, J. M. & Roueff, E. 1977, A&A, 56, 289
Liszt, H. S. & Lucas, R. 1998, A&A, 339, 561
Madden, S. C., Poglitsch, A., Geis, N., Stacey, G. J., & Townes, C. H. 1997, ApJ, 483, 200
Maloney, P. & Black, J. H. 1988, ApJ, 325, 389
McClure-Griffiths, N. M., Dickey, J. M., Gaensler, B. M., et al. 2012, ApJS, 199, 12
McClure-Griffiths, N. M., Dickey, J. M., Gaensler, B. M., et al. 2005, ApJS, 158, 178
Molinari, S., Swinyard, B., Bally, J., et al. 2010, A&A, 518, L100
Nakagawa, T., Yui, Y. Y., Doi, Y., et al. 1998, ApJS, 115, 259
Ossenkopf, V., Röllig, M., Neufeld, D. A., et al. 2012, ArXiv e-prints
Ott, S., Bakker, J., Brumfitt, J., et al. 2006, in Astronomical Society of the Pacific Conference Series, Vol. 351, Astronomical Data Analysis Software and Systems XV, ed. C. Gabriel, C. Arviset, D. Ponz, & S. Enrique, 516
Paradis, D., Dobashi, K., Shimoikura, T., et al. 2012, A&A, 543, A103
Peek, J. E. G., Heiles, C., Douglas, K. A., et al. 2011, ApJS, 194, 20
Petuchowski, S. J. & Bennett, C. L. 1993, ApJ, 405, 591
Pikel'Ner, S. B. 1968, Soviet Ast., 11, 737
Pilbratt, G. L., Riedinger, J. R., Passvogel, T., et al. 2010, A&A, 518, L1+
Pineda, J. L., Goldsmith, P. F., Chapman, N., et al. 2010a, ApJ, 721, 686
Pineda, J. L., Ott, J., Klein, U., et al. 2009, ApJ, 703, 736
Pineda, J. L., Velusamy, T., Langer, W. D., et al. 2010b, A&A, 521, L19
Planck Collaboration, Ade, P. A. R., Aghanim, N., et al. 2011, A&A, 536, A19
Rachford, B. L., Snow, T. P., Tumlinson, J., et al. 2002, ApJ, 577, 221
Reynolds, R. J. 1989, ApJ, 339, L29
Roelfsema, P. R., Helmich, F. P., Teyssier, D., et al. 2012, A&A, 537, A17
Rolleston, W. R. J., Smartt, S. J., Dufton, P. L., & Ryans, R. S. I. 2000, A&A, 363, 537
Roman-Duval, J., Jackson, J. M., Heyer, M., Rathborne, J., & Simon, R. 2010, ApJ, 723, 492
Rubio, M., Garay, G., Montani, J., & Thaddeus, P. 1991, ApJ, 368, 173
Sakamoto, S. 1996, ApJ, 462, 215
Sanders, D. B., Scoville, N. Z., Tilanus, R. P. J., Wang, Z., & Zhou, S. 1993, in American Institute of Physics Conference Series, Vol. 278, Back to the Galaxy, ed. S. S. Holt & F. Verter, 311–314
Savage, C., Apponi, A. J., Ziurys, L. M., & Wyckoff, S. 2002, ApJ, 578, 211
Scoville, N. Z. & Sanders, D. B. 1987, in Astrophysics and Space Science Library, Vol. 134, Interstellar Processes, ed. D. J. Hollenbach & H. A. Thronson, Jr., 21–50
Solomon, P. M. & Klemperer, W. 1972, ApJ, 178, 389
Stacey, G. J., Geis, N., Genzel, R., et al. 1991, ApJ, 373, 423
Steiman-Cameron, T. Y., Wolfire, M., & Hollenbach, D. 2010, ApJ, 722, 1460
Stil, J. M., Taylor, A. R., Dickey, J. M., et al. 2006, AJ, 132, 1158
Taylor, A. R., Gibson, S. J., Peracaula, M., et al. 2003, AJ, 125, 3145
Tielens, A. G. G. M. 2005, The Physics and Chemistry of the Interstellar Medium
Vallée, J. P. 2008, AJ, 135, 1301
van der Tak, F. F. S., Black, J. H., Schöier, F. L., Jansen, D. J., & van Dishoeck, E. F. 2007, A&A, 468, 627
van Dishoeck, E. F. & Black, J. H. 1988, ApJ, 334, 771
Vázquez-Semadeni, E. 2012, in EAS Publications Series, Vol. 56, EAS Publications Series, ed. M. A. de Avillez, 39–49
Velusamy, T., Langer, W. D., Pineda, J. L., et al. 2010, A&A, 521, L18
Velusamy, T., Langer, W. D., Willacy, K., Pineda, J. L., & Goldsmith, P. F. 2013, in IAU Symposium, Vol. 292, IAU Symposium, 235–238
Visser, R., van Dishoeck, E. F., & Black, J. H. 2009, A&A, 503, 323
Whittet, D. C. B., Goldsmith, P. F., & Pineda, J. L. 2010, ApJ, 720, 259
Wilson, C. D. 1995, ApJ, 448, L97
Wilson, N. J. & Bell, K. L. 2002, MNRAS, 337, 1027
Wolfire, M. G. 2010, Highlights of Astronomy, 15, 409
Wolfire, M. G., Hollenbach, D., & McKee, C. F. 2010, ApJ, 716, 1191
Wolfire, M. G., Hollenbach, D., McKee, C. F., Tielens, A. G. G. M., & Bakes, E. L. O. 1995, ApJ, 443, 152

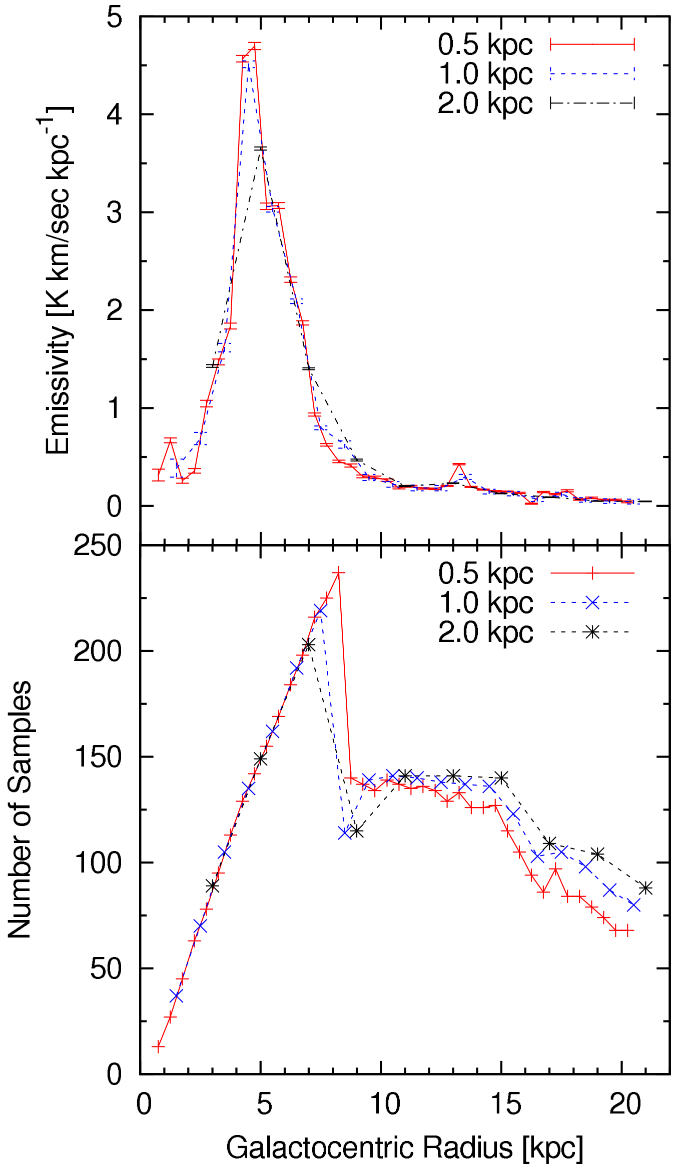

Fig. A.2. (*top*) Radial distribution of the [C II] emissivity for different values of the radial extent for each ring $\Delta R = 0.5$ kpc, 1 kpc, and 2 kpc. (*bottom*) The number of samples crossed by the GOT C+ lines–of–sight as a function of Galactocentric radius, for different values of ΔR.

Wolfire, M. G., Hollenbach, D., & Tielens, A. G. G. M. 1989, ApJ, 344, 770
Wolfire, M. G., McKee, C. F., Hollenbach, D., & Tielens, A. G. G. M. 2003, ApJ, 587, 278

Appendix A: Azimuthally averaged line emissivities

In the following we describe the procedure we used to calculate the radial distribution of the azimuthally averaged integrated intensity per unit length of a spectral line. Assuming a flat rotation curve and circular motions, the distance to the Galactic center R for a given data point with Galactic longitude l, latitude b, and local standard of rest (LSR) velocity $V_{\rm LSR}$, is given by

$$R = R_{\odot}\left(1 + \frac{V_{\rm LSR}}{V_{\odot}\sin(l)\cos(b)}\right)^{-1}, \qquad (A.1)$$

where $R_{\odot}$ is the distance from the sun to the Galactic center and $V_{\odot}$ is the orbital velocity of the sun with respect to the Galactic center. We adopt the IAU recommended values of $R_{\odot} = 8.5$ kpc and $V_{\odot} = 220$ km s^{-1}. We can invert Equation (A.1) to relate the observed LSR velocity of the emission to the Galactocentric distance through

$$V_{\rm LSR} = V_{\odot}\sin(l)\cos(b)\left(\frac{R_{\odot}}{R} - 1\right). \qquad (A.2)$$

We divided the Galaxy in a set of concentric rings, with a central radial distance R and a radial extent $\Delta R = R_{\rm out} - R_{\rm in}$. For a given ring, we used Equation (A.2) to calculate the corresponding interval limits in $V_{\rm LSR}$. We then calculated the integrated intensity $I(l, R)$ within this LSR velocity range. The integrated intensity depends on the path length crossed by a given line of sight, $L(l, R_{\rm out}, R_{\rm in})$, and therefore we divided by this path length to calculate the integrated intensity per unit length (emissivity). The units of the emissivity are K km s^{-1} kpc^{-1}. The value of L depends on the location of the Galaxy we are sampling. This dependency is illustrated in Figure A.1 where we show a schematic of the different cases we considered for the calculation of L.

In Case 1a we considered rings with outer radii inside the solar circle ($R_{\rm out} \leq R_{\odot}$) and inner radius $R_{\rm in}$ larger than the radius of the tangent $R_{\rm tan} = |R_{\odot}\sin(l)|$. In this case a given ring is crossed twice by a given LOS. The path length for one of these crossings is given by,

$$L = \sqrt{(R_{\rm out})^2 - (R_{\rm tan})^2} - \sqrt{(R_{\rm in})^2 - (R_{\rm tan})^2}. \qquad (A.3)$$

In Case 1b we considered rings with $R_{\rm in} < R_{\rm tan} \leq R_{\rm out}$. In this case a ring is crossed only once and the path length is given by,

$$L = 2\sqrt{(R_{\rm out})^2 - (R_{\rm tan})^2}. \qquad (A.4)$$

In Case 2 we considered LOSs that cross rings in the outer Galaxy with $R_{\rm in} > R_{\odot}$. These rings are crossed once and the path length is given by Equation (A.3).

Rings in Case 3a have $R_{\rm in} < R_{\odot} < R_{\rm out}$ and are observed in LOSs in the range $270° > l > 90°$. In this case the path length is given by the distance to the point with $R = R_{\rm out}$,

$$L = R_{\odot}\cos(l) + \sqrt{(R_{\rm out})^2 - (R_{\rm tan})^2}. \qquad (A.5)$$

Finally for Case 3b, we considered rings with $R_{\rm in} < R_{\odot} < R_{\rm out}$ observed in LOSs in the range $270° < l < 90°$. In this case we cross a ring twice. For the near side the path length is given by

$$L = R_{\odot}\cos(l) + \sqrt{(R_{\rm in})^2 - (R_{\rm tan})^2}, \qquad (A.6)$$

and for the far side is given by Equation (A.3).

The final step is to average the emissivities over all samples of a given ring. This sum is done over all rings sampled by the GOT C+ survey N_s,

$$I_0(R) = \frac{\sum_i^{N_s} I_i/L_i}{N_s}. \qquad (A.7)$$

We estimated the errors on the emissivity by propagating the errors of the individual determinations of the integrated intensity per unit length, $\Delta I/L$, using,

$$\Delta I_0(R) = \frac{\sqrt{\sum_i^{N_s}(\Delta I_i/L_i)^2}}{N_s}. \qquad (A.8)$$

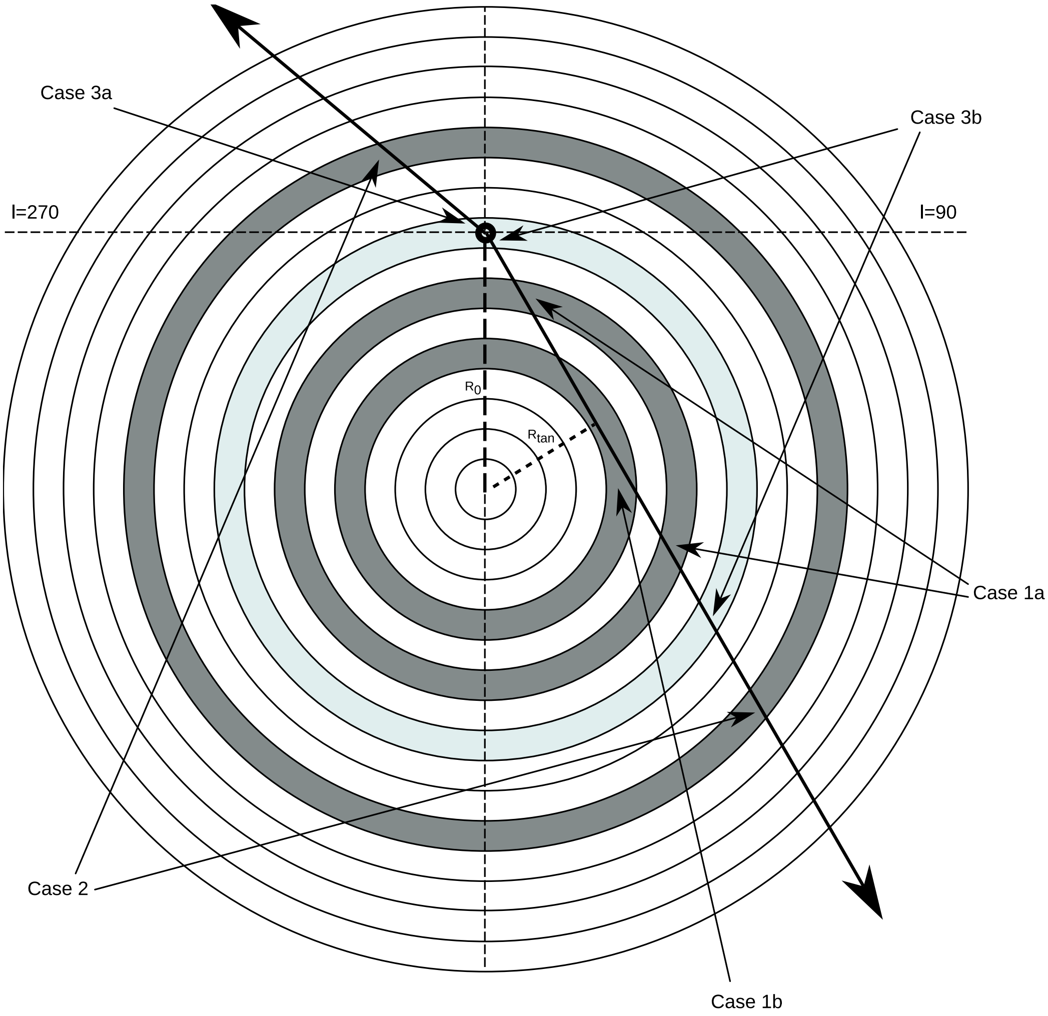

Fig. A.1. Schematic of the Milky Way divided by a set of rings centered at the Galactic center. The two thick arrows originating from the Sun (shown as a circle) correspond to two lines–of–sight, one looking toward the inner Galaxy and the other toward the outer Galaxy. The dashed lines represent the distance to the Galactic center ($R_{\odot}$) and the distance to the tangent point ($R_{\rm tan}$) for the line of sight that goes towards the inner Galaxy. The thin lines point to the different path lengths crossed by the lines–of–sight that correspond to the different cases considered in the text.

In the top panel of Figure A.2 we show the resulting radial distribution of the [C ii] emissivity for different values of $\Delta R = 0.5$ kpc, 1 kpc, and 2 kpc. We can see that for larger values of ΔR the peak shifts to around 5 kpc, which is the midpoint where most of the [C ii] emission observed in the GOT C+ survey arises in the Galaxy. We adopt $\Delta R = 0.5$ kpc to preserve the details of the [C ii] emissivity distribution. The uncertainty in the [C ii] emissivities for this selection of ΔR is typically 0.02 K km s^{-1} kpc^{-1}. The bottom panel shows the number of samples (N_s) for a given ring. As we can see, rings with radii below 2 kpc are undersampled in our survey. Given that such rings are sampled by lines–of–sights with $|l| < 3°$, and that these LOSs are also known to have non-circular motions, we exclude these LOSs in our analysis. This exclusion has a minimal effect on emissivity distribution beyond 2 kpc.

Appendix B: Position–velocity maps

In Figures B.1 to B.4, we present the position–velocity maps of the [C ii], CO, and H i emission for the GOT C+ lines–of–sight with $b = \pm0.5°$ and $b = \pm1.0°$. Figure B.5 shows the position–velocity maps for the different cloud types discussed in Section 4.1, for the GOT C+ lines–of–sight with $b = \pm0.5°$ and $b = \pm1.0°$.

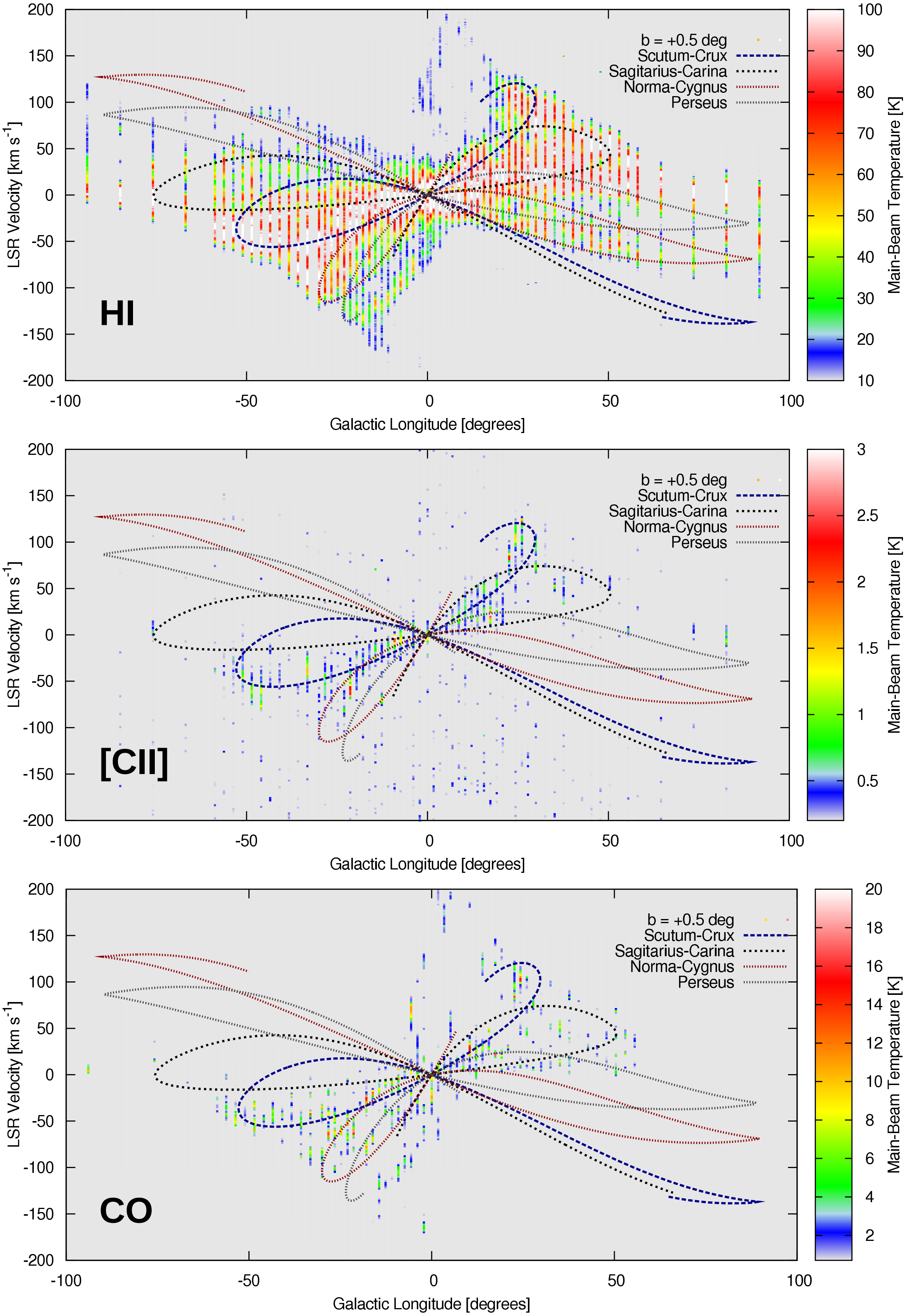

Fig. B.1. Position–velocity maps of the Milky Way in [C ɪɪ] observed by GOT C+ for $b = +0.5°$.

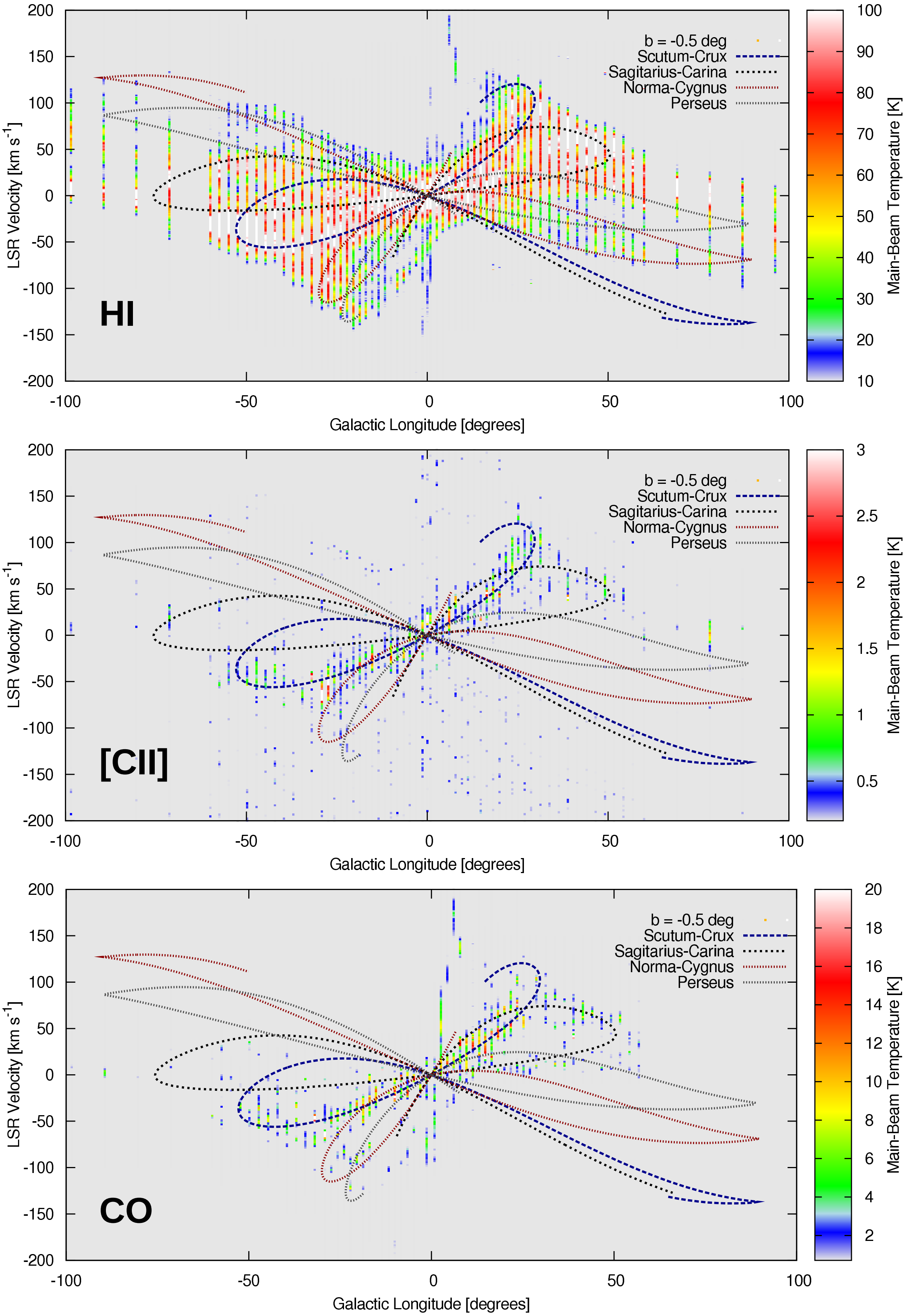

Fig. B.2. Position–velocity maps of the Milky Way in [C II] observed by GOT C+ for $b = -0.5°$.

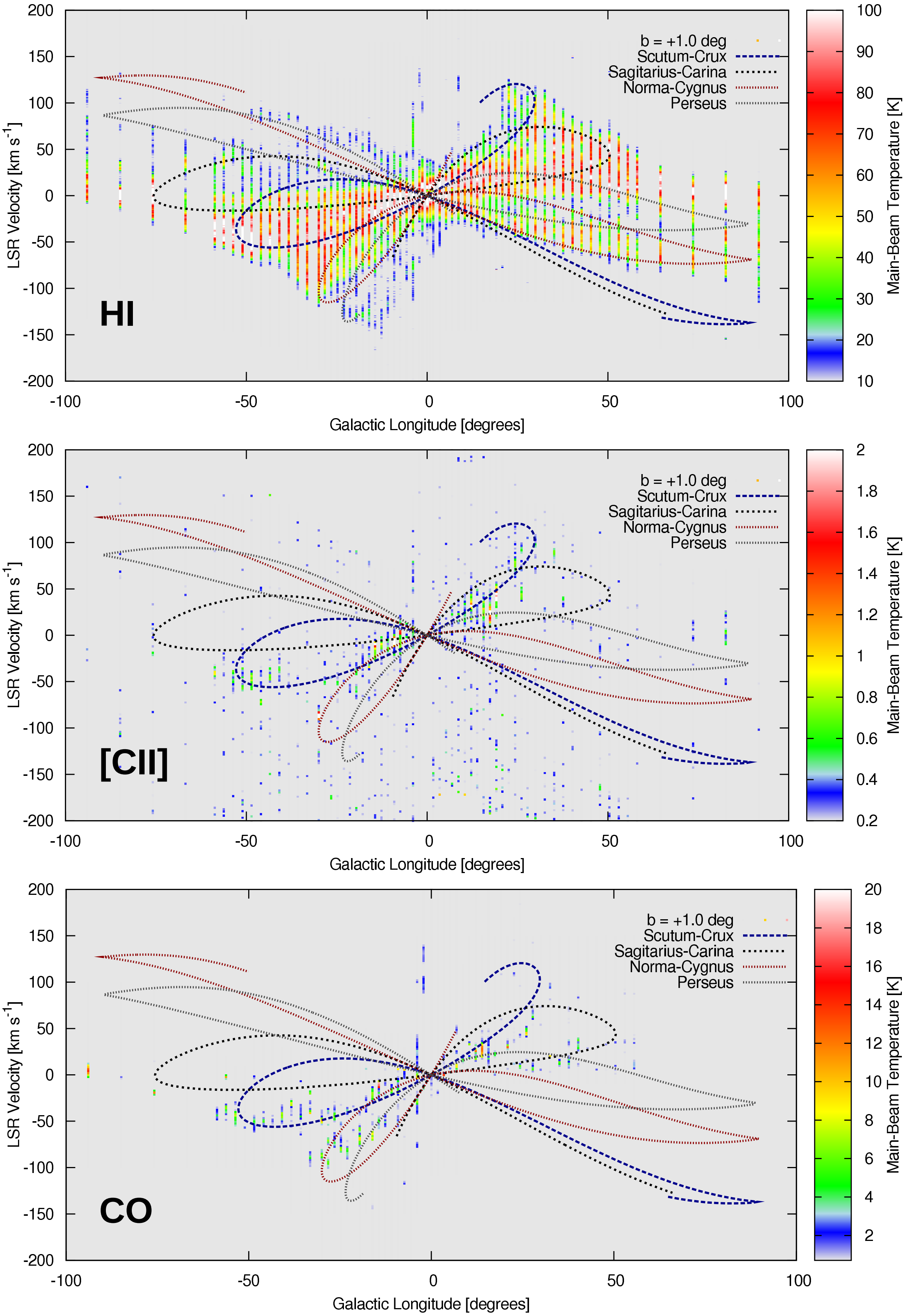

Fig. B.3. Position–velocity maps of the Milky Way in [C ii] observed by GOT C+ for $b = +1.0°$.

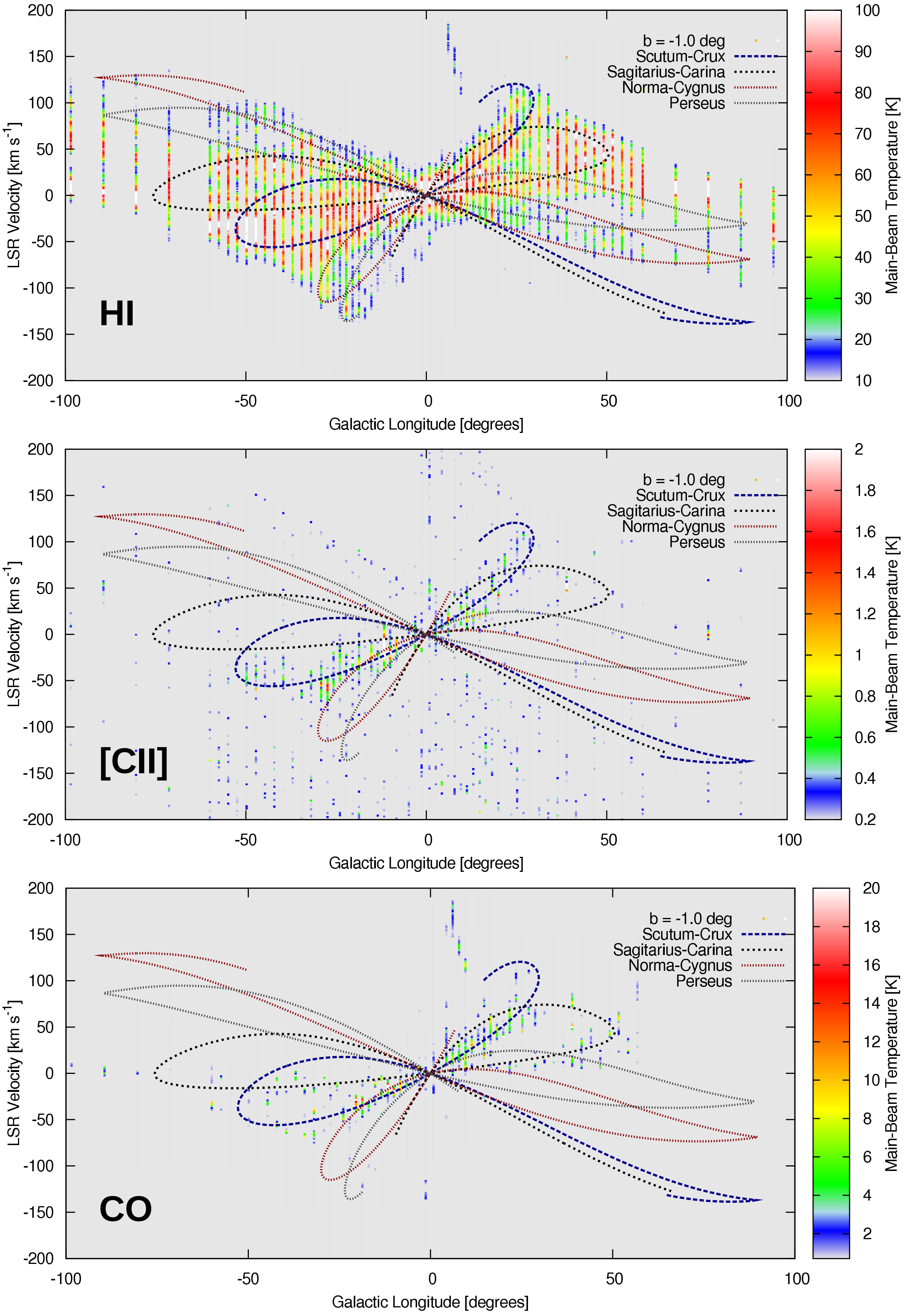

Fig. B.4. Position–velocity maps of the Milky Way in [C II] observed by GOT C+ for $b = -1.0°$.

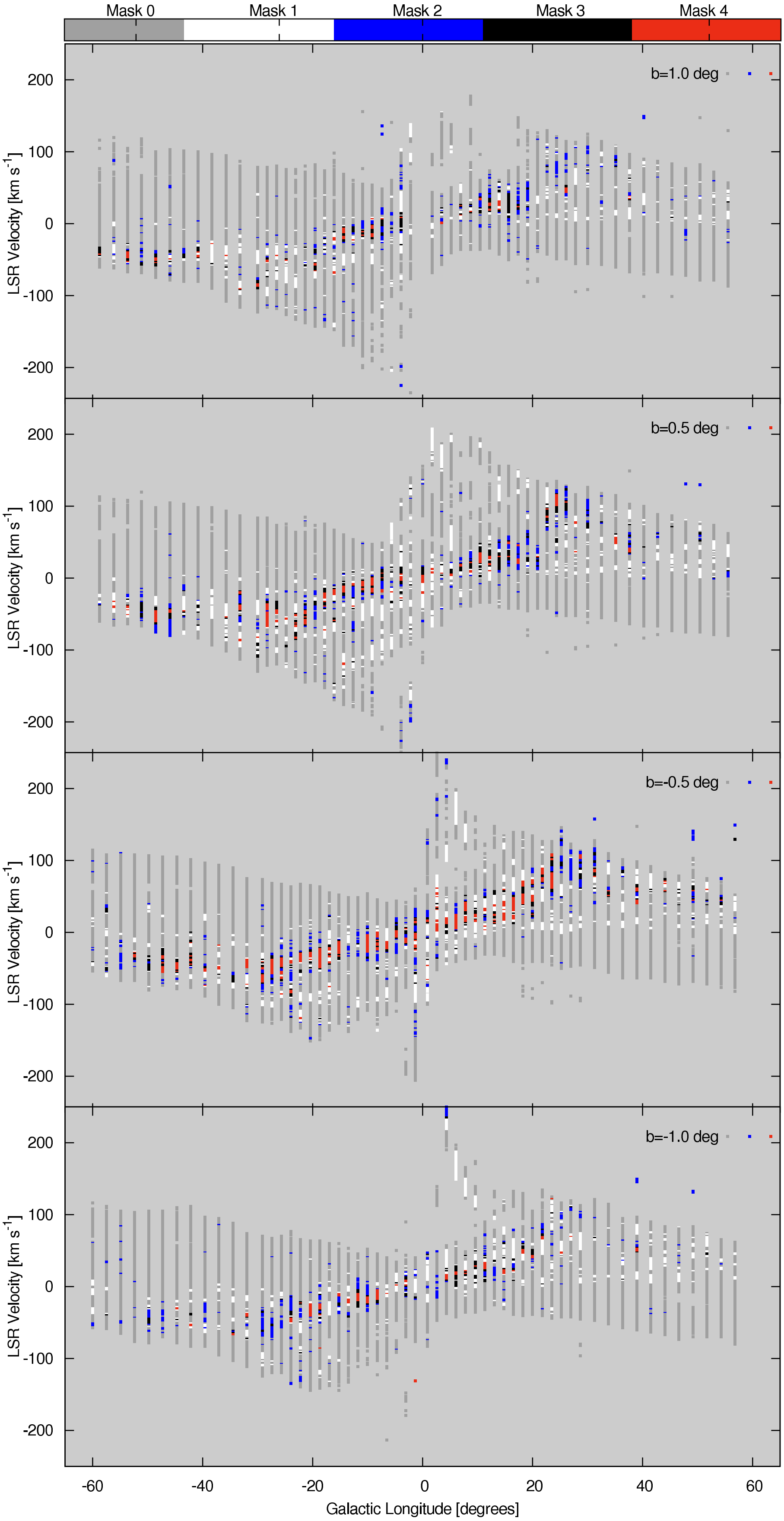

Fig. B.5. Position velocity maps of the different cloud types defined in Section 4.1 for $b = \pm0.5°$ and $\pm1.0°$. The Mask 0 (*grey*) represents velocity components with only H ɪ detected, Mask 1 (*white*) are components with only H ɪ and CO detected, Mask 2 (*blue*) components with only H ɪ and [C ɪɪ], Mask 3 (*black*) components with H ɪ, [C ɪɪ], and CO, and Mask 4 (*Red*) components with H ɪ, [C ɪɪ], ^{12}CO, and ^{13}CO.